Nano Energy 99 (2022) 107424

Contents lists available at ScienceDirect

Nano Energy

journal homepage: www.elsevier.com/locate/nanoen

Prussian blue and its analogues as cathode materials for Na-, K-, Mg-, Ca-, Zn- and Al-ion batteries

Yujie Yang [a,b,1], Jianbin Zhou [c,1], Linlin Wang [a,*], Zheng Jiao [d,*], Meiyi Xiao [b], Qiu-an Huang [a], Minmin Liu [a], Qinsi Shao [a], Xueliang Sun [e], Jiujun Zhang [a,*]

[a] Institute for Sustainable Energy/College of Science, Shanghai University, Shanghai 200444, PR China
[b] School of Environmental and Chemical Engineering, Shanghai University, Shanghai 200444, PR China
[c] Hefei National Laboratory for Physical Science at Microscale and Department of Chemistry, University of Science & Technology of China, Hefei, Anhui 230026, PR China
[d] Shanghai Applied Radiation Institute, Shanghai University, Shanghai 201800, PR China
[e] Department of Mechanical and Materials Engineering, University of Western Ontario, 1151 Richmond St, London, Ontario N6A 3K7, Canada

ARTICLE INFO

Keywords:
Prussian blue and its analogues
Cathodes
Low-cost metal-ion batteries
Aqueous and non-aqueous batteries

ABSTRACT

Prussian blue and its analogs (PB/PBAs) are competitive candidates for cathode materials of rechargeable metal-ion batteries (monovalent metal such as Na and K and multivalent metal, e.g. Mg, Ca, Zn, and Al) due to their stable frame structures, tunable redox sites, and facile synthesis methods. This paper comprehensively reviews the research progress of PB/PBAs-based cathode materials of metal-ion batteries in terms of their synthesis, structural/composition characteristics, electrochemical performance, functional mechanisms, applications and recycling in electrical energy storage. For facilitating the research and development, some technical challenges are analyzed and future research directions are also proposed for overcoming the challenges toward their practical applications.

1. Introduction

With the increased energy demand, the consumption of fossil fuels for energy is accelerated, causing the fast depletion of fossil fuels and the associated environmental impact. To avoid possible energy crises and environmental pollution, safe, efficient, and clean energy supplies from sustainable solar, wind, waterfall, geothermal and so on are highly needed. However, the electrical energy generated from these sources is usually intermittent and requires electrochemical energy devices (EEDs) to make it stored for grid applications [1]. In this sense, EEDs including batteries, supercapacitors and water electrolyzers for producing hydrogen have attracted much attentions in the most recent years [2–5]. Particularly, lithium-ion batteries (LIBs) have become the major energy/power sources for smart electronic devices and electric vehicles. However, the scarce lithium resources are becoming a barrier to limit the large-scale and sustainable applications of lithium-ion batteries [6]. To mitigate this issue, a series of other types of metals such as Na^+, K^+, Mg^{2+}, Ca^{2+}, Zn^{2+}, Al^{3+}, etc. have been explored as the potential metal-ion batteries. Compared with lithium, the above-mentioned metals have obvious advantages in terms of cost and abundance (Fig. 1). For cathode materials of such metal-ion batteries, many types of materials including ($Na_3V_2(PO_4)_3$ [7], $Na_2FeFe(CN)_6$ [8], $KFeFe(CN)_6$ [9], $K_{0.5}MnO_2$ [10] etc.) have been employed to achieve high energy/-power densities and cycling life.

As recognized, cathode materials, the critical components of metal-ion batteries, determine the capacities of the batteries to a large extent and the upper limit of the cell voltage and restrict the overall energy/power densities as well as the safety of the batteries. Taking sodium-ion batteries (SIBs) and potassium-ion batteries (PIBs) as examples, the currently used positive electrode materials are mainly layered metal oxides, polyanionic compounds, Prussian blue analogues, and organic compounds etc.

The layered metal oxides have been extensively studied in metal-ion batteries. However, the repeated intercalation of metal ions can lead to volume expansion and sliding between transition metal layers during charging and discharging and finally battery failure. Furthermore, the increasing cost for metals such as Co/Ni can be a hindrance to large-scale application. Moreover, ions with larger radius such as sodium

* Corresponding authors.
E-mail addresses: wlinlin@mail.ustc.edu.cn (L. Wang), zjiao@shu.edu.cn (Z. Jiao), jiujun.zhang@i.shu.edu.cn (J. Zhang).
[1] These authors contributed equally to the work

https://doi.org/10.1016/j.nanoen.2022.107424
Received 15 February 2022; Received in revised form 16 May 2022; Accepted 22 May 2022
Available online 25 May 2022

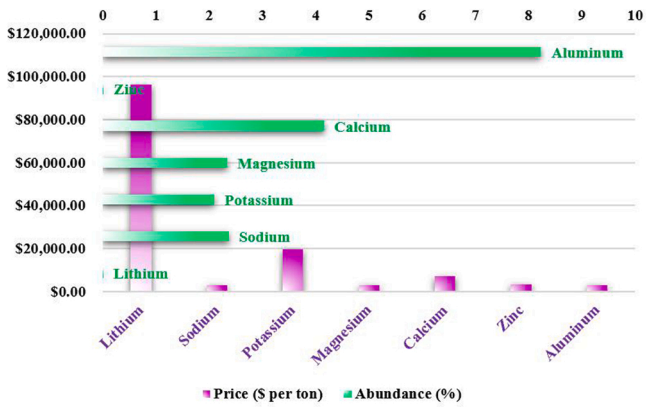

Fig. 1. Comparison of metal prices and abundance of the earth's crust.

and potassium ions, are more likely to cause structural collapse during intercalation. For polyanionic compounds, they have thermodynamic stability and high operating voltage, but their initial specific capacities are relatively is low, and are prone to phase transformation under high potential. Organic cathode materials can provide high reversible capacities, but they are easy to be dissolved in organic electrolytes, leading to poor cycling stability.

Among numerous organic/inorganic cathode materials, Prussian blue (PB) and its analogs (PBAs), a kind of metal organic frameworks (MOFs) with intrinsic metal existence and ordered interconnection structures have stood out [11–13]. Compared with layered metal oxides and polyanionic compounds, PB lattice has a larger gap A site diameter (4.6 Å) that enables large metal ions to insert, and the internal three-dimensional network structure can reduce structure change caused by the repeated intercalation of metal ions, which has been identified to a promotion cathode material for metal-ion batteries [14, 15] (Fig. 2). Furthermore, the PB/PBAs with tunable composition and customizable framework can meet the requirements of different batteries applications [16].

The development of PB and PBAs has been explored for non-aqueous and aqueous metal ion batteries and has shown to be promising for practical applications [17]. In this review, we mainly summarize the synthesis of PB/PBAs, their characterization, functional mechanisms, the current status of their applications and recycling in low-cost metal-ion batteries. The technical challenges facing PB/PBAs material development are analyzed, and several possible future research directions are also proposed for overcoming the challenges toward their practical applications. We hope that this review could facilitate the research and development of PB/PBAs cathode materials of metal-ion batteries for commercial application.

2. Structure characteristics, working principle, and synthesis method

2.1. Structural characteristics

The chemical structures of PB/PBAs can be described with a general chemical formula: $A_xM_A[Fe(CN)_6]_{1-y}\cdot\square_y\cdot nH_2O$ $(0 < x < 2; y < 1)$, in which A usually represents the guest ions, such as Li^+, Na^+, K^+, etc.; M_A usually represents transition metal ions coordinated with nitrogen, while Fe is coordinated with carbon; □ is vacancy for $[Fe(CN)_6]$ [18]. PB

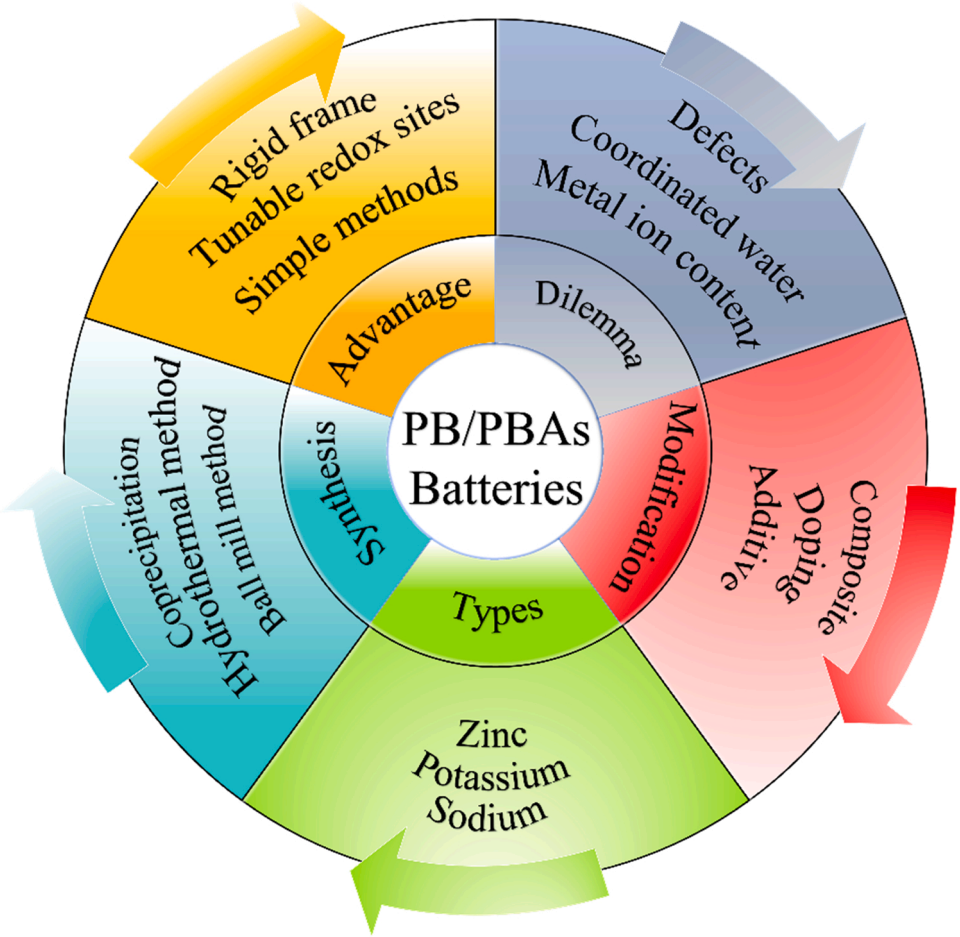

Fig. 2. Illustration of the research progresses of PBAs in batteries.

is an iron centered compound, while PBAs are a kind of chemical composition with partially or completely replacing the iron center with different metal ions (Co, Ni, Mn, Zn, Cu, etc.) [19]. The crystal structure of PB was firstly confirmed in 1936 with a face-centered cubic structure based on the analysis of powder X-ray diffraction pattern. More information on PB structure was elucidated in the next few years [20–22]. PB/PBAs represent a series of transition-metal hexacyano complexes with perovskite-type face-centered cubic structures (whose space group is $Fm\bar{3}m$) [23]. This group is composed of two structure characteristics (Fig. 3a). The first one is an insoluble form ($Fe_3[Fe(CN)_6]_2{\cdot}xH_2O$, x = 14–16), in which the water molecule is usually coordinated with the metal center to balance the charge difference caused by the defect. The second one is the soluble form ($A_{4-y}Fe_y[Fe(CN)_6]{\cdot}zH_2O$, y = 0–1) with the metal ions residing in the lattices [20,24]. The interstitial position in this open structure (~4.6 Å) is more than enough to accommodate a certain amount of metal ions (such as Na^+, K^+, Rb^+, Cs^+, Mg^{2+}, Ca^{2+}, Zn^{2+}, Al^{3+}, etc.) as well as water molecules [25]. Nordstrand et al. [26] studied the ion transport mechanism of intercalated cations in PBA materials by using a multi-scale modeling method, revealing the ladder mechanism of cation transport, in which the diagonal movement of the embedded cations between internal planes within a crystal cell was surrounded by four negatively charged CN groups. These CN groups enabled as the steps for ions to climb into the crystal. Similarly, all the frames around the CN frame could brace embedded ions. The entire channel barriers for the movement of embedded ions could increase as the part of frame was damaged by a vacancy. Peng et al. [27] further studied Na^+ storage and migration mechanism in the defect-rich and intact structure by using density functional theory (DFT) calculations. As shown in Fig. 3b, two possible Na^+ migration paths are proposed to understand the Na^+ migration mechanism in both defect-rich (left) and intact (right) crystal structures: In Path 1, Na^+ migration along the axis through the defect/unit center; and in Path 2, Na^+ migration bypasses the nearest defect/unit center along the s-migration path. The corresponding Na^+ migration energy barrier is presented in Fig. 3c. Path 2 shows the low energy barrier in both defect-rich and intact crystal structures, indicating that the insertion of Na^+ is more like S-shaped path. Moreover, the calculations also indicate that the energy barrier of intact crystal structure is lower than the defect-rich crystal structure. However, there are still some controversies about ion migration paths inside the PBAs.

2.2. Working principles

The electrochemical properties of PB/PBAs are closely related to the valences and spin states of transition metal elements M_A and Fe, the number of vacancies in the lattice and the crystal water content. In the coordination structure of Fe-C≡N-M_A, the nitrogen in the M_AN_6 octahedron is a weak ligand, resulting in the high spin (HS) of the central ion M_A, while the carbon in the FeC_6 is a strong ligand, resulting in the low spin (LS) of the central ion Fe [28]. The different states of electron spin can affect the capacity contribution in electrochemistry. The PB/PBAs synthesized by co-precipitation in the liquid phase commonly contain a large number of randomly distributed $Fe(CN)_6$ vacancies. The number of vacancies is related to the valence relationship between M_A and Fe. Fig. 3d shows a defect-free PB cubic lattice and a defective one. According to the stoichiometric ratio relations (3:4 of Fe^{2+} and Fe^{3+} sites) and electrically neutral principle, the lattice contains within 25% $[Fe^{II}(CN)_6]^{4-}$ vacancies. These defects can be occupied by the coordinated water. In addition, there is also a certain amount of interstitial water in the lattice cavities. Therefore, transition metals near the vacancies are prone to coordinate with water molecules during the intercalation process of guest ions, leading to lattice distortion, weak ability to store guest ions, and poor electrochemical performance [29].

The electrochemical activity of PBAs in metal ion batteries is mainly derived from the redox-active centers of transition metal M_A and Fe, and the valence change of transition metal ions during the insertion of guest

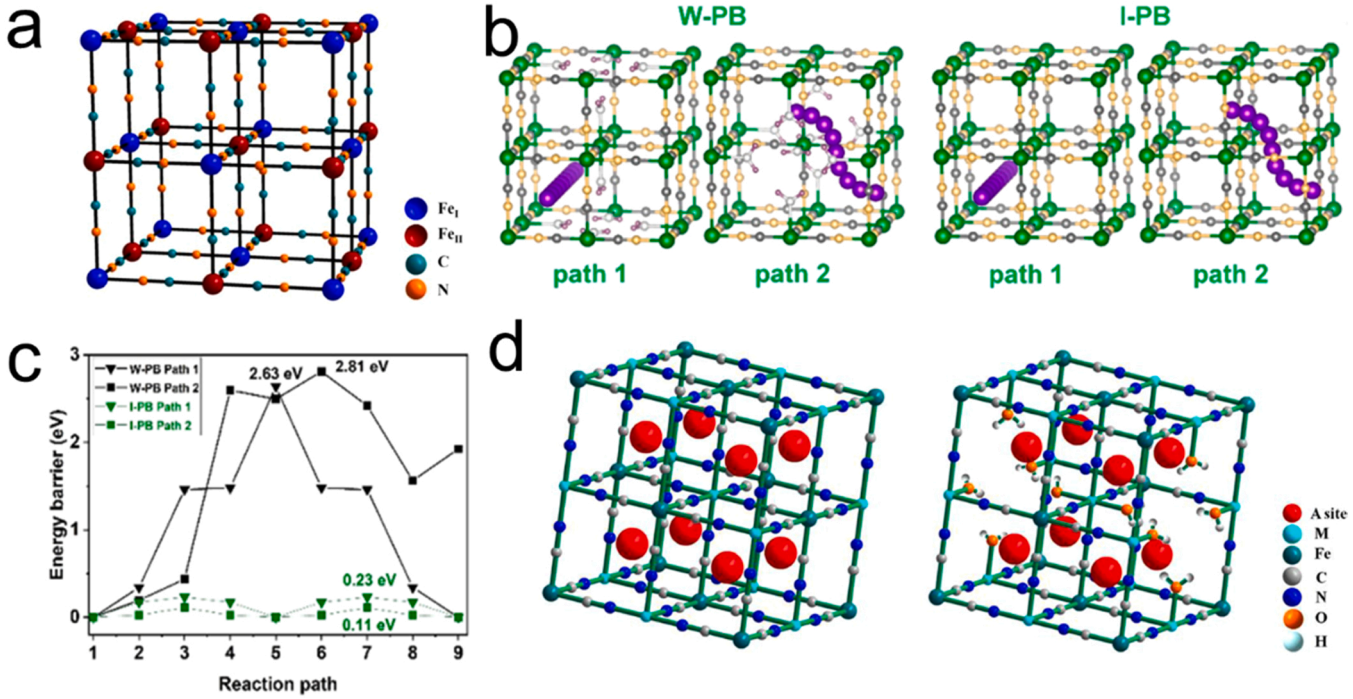

Fig. 3. (a) Schematic representation of PB ($Fe[Fe(CN)_6]$) frameworks. Reprinted with permission [30]. Copyright 2016, American Chemical Society. (b) Two possible Na^+ migration paths inside the defect-rich crystal structure of W-PB and the defect-free crystal structure of I-PB (green ball: Fe; gray ball: C; yellow ball: N; purple ball: Na) [27]. Copyright 2022, American Chemical Society. (c) Corresponding migration energies of the two paths in W-PB and I-PB [27]. Copyright 2022, American Chemical Society. (d) Crystal structures of PBAs: an intact $Na_2M^{II}[Fe^{II}(CN)_6]$ framework without structural defects and an ideally defective $NaM^{II}[Fe^{II}(CN)_6]_{0.75}{\bullet}\square_{0.25}$ framework with 25% $Fe(CN)_6$ vacancies existing in each unit cell. Reprinted with permission[31]. Copyright 2016, American Chemical Society.

ions. Generally, PBAs can be denoted as M_AFe-PBA [32]; (i.e. NiFe-PBA, FeFe-PBA, MnFe-PBA, CuFe-PBA, CoFe-PBA, ZnFe-PBA, VFe-PBA, etc.). Therefore, the energy storage mechanism can be divided into two categories according to the different electrochemical activities of the transition metal M_A: one is the single-electron redox reactions represented by electrochemical inert metal elements such as Ni, Cu, and Zn [18]; the other one is the multi-electron redox reactions represented by the electrochemical active metal elements such as Fe, Mn, Co, and V [33].

The special crystal structure of PBAs has established its role in electrochemical energy storage and exhibited its unique advantages: (1) the rigid frame structures and open active sites can provide wide 3D channels for the intercalation and deintercalation of guest ions; (2) the presence of the transition metals can provide the multi-electron redox reactions, which can deliver higher theoretical capacities than other electrode materials [34].

2.3. Synthesis methods and their industrialization evaluation

Due to the relatively simple synthesis methods, low preparation cost, and environmental friendliness, PB/PBAs have superiority in metal-ion batteries, and also provide a broad prospect for industrialized production.

By summarizing the previous reports, the preparation methods of PB/PBAs are listed in the following categories:

a. Co-precipitation method. The transition metal salt is usually used for solution reaction with $[Fe(CN)_6]^{4-}$ or $[Fe(CN)_6]^{3-}$. The factors affecting the synthesis include the concentration of reaction solution, mixing mode, reaction time, reaction temperature, and the addition of chelating agent. For instance, Zhang et al. [9] prepared $K_{0.220}Fe[Fe(CN)_6]_{0.805}\cdot 4.01H_2O$ nanoparticles by a simple co-precipitation method and used it as the cathode material of PIBs. This cathode electrode delivered a discharge voltage of 3.1–3.4 V with a reversible capacity of 73.2 mAh g^{-1}. However, co-precipitation without any addition is easy to cause defects in PBAs due to the rapid precipitation rate [35]. These defects can seriously affect the ion storage properties and lead to several issues, as follows: (1) a large number of water molecules can coordinate with the unsaturated bonds at the defects, which are easily decomposed by oxidation at high potential, resulting in a decrease of guest ion insertion capacity [11,18]; (2) water molecules can occupy part of ion intercalation sites and block ion transport channels, leading to slow ion kinetics [26]; (3) the lattice distortion or bond fracture can be resulted from the process of the repeated ion deintercalation, leading to serious attenuation of the cycling performance [8]. Nowadays, the addition of sodium citrate or potassium citrate has previously been reported to successfully prepare lowdefect PB/PBAs, which enables the optimized co-precipitation to be a potential large-scale production method [33,36,37].

b. Single source method. PB/PBAs can be synthesized through the decomposition and recombination of ferricyanide itself. $[Fe(CN)_6]^{4-}$ slowly decomposes in an acidic solution and releases Fe^{2+} which would react with the remaining $[Fe(CN)_6]^{4-}$ to obtain PB/PBAs with regular morphology. You et al. [29] synthesized a highly crystalline $Na_{0.61}Fe[Fe(CN)_6]_{0.94}$ as the cathode material for SIBs. The reversible capacity of this material was about 170 mAh g^{-1} at 25 mA g^{-1} with the coulombic efficiency close to 100%. R-$Na_{1.92}Fe[Fe(CN)_6]$ with the rhombohedral phase was synthesized by Wang et al. [38] through the single iron source method. When assembled into SIBs, this material delivered a high specific capacity and long cycling life. An initial discharge capacity of 157 mAh g^{-1} at 15 mA g^{-1} and a high capacity retention of 80% after 750 cycles at 300 mA g^{-1} were achieved. Liu et al. [39] fabricated PB cathodes for SIBs with concave center cubic, which showed both good cycling stability and rate performance and could achieve a specific capacity of 107 mAh g^{-1} at 0.2 A g^{-1}. The material obtained by this reaction possessed the characteristics of low defect content and high crystallinity, but the yield of the PB-derived materials was relatively low. Furthermore, the method can often produce toxic CN^- during synthesis. Therefore, it is limited to be applied in large-scale industrialization production [40,41].

c. Electrochemical deposition. The electrochemical deposition (electrodeposition) of PBAs can be performed by using the three-electrode system. For instance, the working electrode is immersed in a solution with $Fe^{3+}/K_3Fe(CN)_6$ to obtain PBAs by performing cyclic voltammetry test within a set range of potential for continuous scanning. The main factors that influence the reaction are the concentration of reaction solution, stirring speed, temperature and surface-active agent. For example, He et al. [42] fabricated $K_2Zn_3(Fe(CN)_6)_2.9H_2O$@CC by an electrochemical deposition method, which was directly used as the self-supporting cathode of SIBs. The obtained results showed a high areal specific capacity of 0.76 mAh cm^{-2} at 0.5 mA cm^{-2}. The method can be widely used to synthesize PB/PBAs composites with different substrates, while the operation and equipments of the methode are quite complicated.

d. Ball-milling method. Ball milling method is a method of solid-phase synthesis, during which transition metal salt and $Na_4Fe(CN)_6\cdot 10H_2O$ are reacted under the protection of inert gas. The crystal water in materials is released during the process of ball-milling to dissolve the reactants to obtain PBAs. The main controlling factors are crystal water contents of reactants, rotating speed, ball grinding time, reaction atmosphere, ball/material ratio, and so on. For example, Gong et al. [43] reported the ultrafine (~40 nm) $Na_{0.9}Fe[Fe(CN)_6]_{0.96}$ nanometer crystals synthesized by ball-milling method and used it as the efficient cathodes for SIBs. A reversible capacity of 106 mAh g^{-1} at 30 C was achieved, and after 500 cycles at 10 C, it still remained 80% of the initial capacity. This method has a high yield and can be applied to large-scale industrial production [44,45].

e. Electrostatic spray assisted coprecipitation (ESAC). In this method, an organic solution containing transition metal salts is first prepared, and then the as-prepared organic solution is sprayed into droplets through a high-voltage electrostatic action, during which the drops go into the reactor with $Fe(CN)_6^{4-}$ or $Fe(CN)_6^{3-}$ for a reaction. For example, Ma et al. [46] synthesized $Na_2Co[Fe(CN)_6]$ nanoparticles by this method and obtained a specific capacity of 154 mAh g^{-1}. The method can obtain low defect crystal, but the equipment is complex and the cost is high, so it is not suitable for industrial production.

Overall, different synthesis methods would have their advantages and disadvantages from different views. To intuitively compare the different methods, we plot a radar map (Fig. 4) with considering the yield, crystallinity, production safety, large-scale production feasibility, production simplicity and cost advantage, which are very important for the practical production of PB/PBAs materials. As shown in Fig. 4, the advantages of co-precipitation and ball milling in various indicators are relatively balanced and applicable to industrial production. It's worth mentioning that the advantages of co-precipitation method are particularly obvious, especially in terms of the yield, production safety, large-scale production feasibility, production simplicity and cost advantage. Although the PB/PBAs prepared by single source method has high crystallinity, toxic CN^- could be produced during the production process, which limits its large-scale production. Other methods, such as electrochemical deposition and electrostatic spray assisted co-precipitation are more complicated and expensive for scale-up production. Therefore, co-precipitation method would hold the promising application for industrial production.

3. The role of PB/PBAs in cathode of metal-ion battery

For metal-ion batteries, the capability of the cathode materials to store ions are one of the critical factors in batteries. In order to obtain

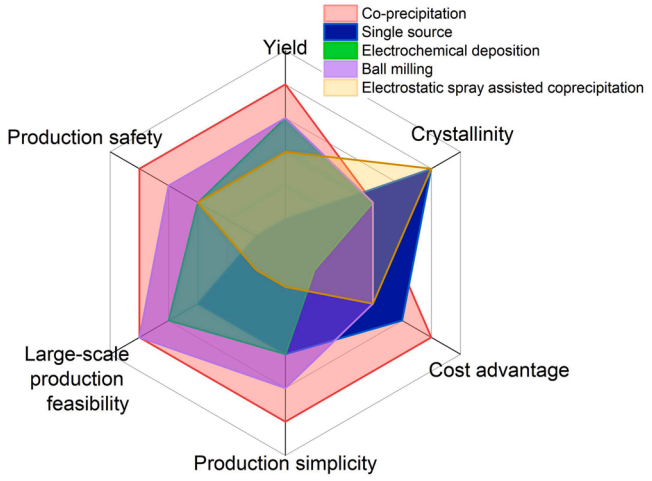

Fig. 4. The radar map of different synthesis methods of PBAs in industrial applications by considering the yield, crystallinity, cost, production simplicity, large scale production feasibility and production safety.

efficient energy storage, several requirements should be qualified by the cathodes: (1) an appropriate spatial structure, which is easy for ion diffusion and electron transfer; (2) structural stability, which is a favor for avoiding structure collapse or large volume change during ion insertion; (3) a high electrode potential to obtain a high operating voltage; (4) simple preparation and environmental friendliness.

It can be seen from the above section that PB/PBAs have obvious advantages in partial synthesis methods: facile synthesis and high yield. However, to determine whether the material has the commercial prospects, analysis of synthesis alone is not enough. The performance and structure analysis must be combined to evaluate the electrochemical properties and the challenges facing PB/PBAs cathode materials for different metal-ion batteries (mainly divided into potential low-cost batteries i.e. sodium-ion and potassium-ion batteries and other low-cost metal-ion batteries i.e. magnesium-ion, calcium-ion, zinc-ion, and aluminum-ion batteries).

3.1. PB/PBAs cathodes in potential low-cost batteries (sodium-ion and potassium-ion batteries)

Monovalent metal ion batteries are important energy storage and conversion devices with great practical and potential application prospects. Among them, lithium-ion batteries have been researched and widely used in our daily life attributed to their advantages of relative high energy/power densities, long cycle-life, and environmental friendliness. However, due to the serious imbalance between the distribution of lithium resources and the increasing demand for lithium resources, the large-scale commercial application of lithium-ion batteries will be severely challenged in the future. In contrast to lithium, both sodium and potassium are abundant and readily available worldwide. In the past large-scale energy storage field, although the research of sodium-ion batteries and potassium ion batteries are not as mature as the lithium-ion batteries, they are still widely studied as the alternatives of lithium-ion batteries. The following sections will introduce the current research status of PB/PBAs in sodium-ion and potassium-ion batteries.

3.1.1. PB/PBAs cathodes in sodium-ion batteries

In the periodic table, lithium and sodium are in the same main group, which leads to their similar physical and chemical properties. Compared with lithium, sodium resources are comparatively rich, with an abundance of 2.74 wt% in the earth's crust (far greater than 0.0002 wt% of lithium), and sodium is easy to mine and low in cost. SIBs have been considered to be a promising alternative for LIBs [47]. However, SIBs still face some challenges: the standard electrode potential of sodium (−2.71 V vs. SHE) is slightly higher than that of lithium-ion (−3.04 V vs. SHE), which results in relatively low operating voltage; and the radius of sodium ion is larger than that of lithium ion, leading to the rapid decline of battery capacity and poor rate capability. Therefore, compared with LIBs, SIBs should have higher requirements for cathode material [48]. However, in terms of large-scale energy storage, the energy storage devices with low cost, high safety, and long lifespan are required, while the energy density demand seem not critical. In this case, sodium-ion batteries would meet the requirements. In this sense, SIBs are expected to replace LIBs as part of the next generation of large-scale energy storage systems [49].

In recent years, PB/PBAs have been the focus for cathode materials of SIBs due to their tunable voltage platform, open three-dimensional ion migration channel, low cost, and non-toxic synthesis methods. PBAs such as $Na_xFe[Fe(CN)_6]$ and $Na_xMn[Fe(CN)_6]$ exhibit the energy densities of 400–520 Wh kg^{-1}, which can rival $LiMn_2O_4$ (430 Wh kg^{-1}) and $LiFePO_4$(~530 Wh kg^{-1}) used in LIBs [18,38,50,51]. Some representative PB/PBAs materials in SIBs applications are summarized in Table 1.

3.1.1.1. PB/PBAs cathodes in non-aqueous sodium-ion batteries. According to the molecular formula of $Na_{2-x}M_A[Fe(CN)_6]_y\square_{1-y}\cdot mH_2O$, wherein □ represents the difference of transition metal elements in Fe$(CN)_6$ vacancy, $0<x<2$, and $0<y<1$. Based on the theoretical double-electron redox reaction, the theoretical capacity of PBAs can be as high as 170 mAh g^{-1} (taking $Na_2FeFe(CN)_6$ as an example) [29], which is twice the theoretical capacity of $Na_4Fe(CN)_6$ (89 mAh g^{-1}) [52]. The electrochemical performances of PBAs are closely related to their intrinsic crystal structures. However, it is difficult for the synthesized PBAs to reach the theoretical capacities. The reasons are followed: (1) the vacancy of $[Fe(CN)_6]$ occupied by coordination water makes Na^+ storage sites inefficient; and (2) the process of Na^+ insertion/extraction may lead to lattice distortion and even the collapse of Fe-C≡N-M_A frame, which further leads to the deterioration of electrochemical performance. These intrinsic properties bring challenges to the fabrication and application of PBAs, driving researchers to optimize the material properties such as crystallinity, defect concentration, and lattice water, etc. to improve their electrochemical performances for sodium-ion battery [19].

Lu et al. [11] synthesized six compounds of $KMFe(CN)_6$ (M=Ni, Mn, Fe, Co, Cu and Zn), and assembled them into sodium-ion half-cells with an organic liquid-carbonate electrolyte. But the lattices of these materials did not contain Na^+. The sodium content was found to closely relate to the electrochemical performance of the battery. For instance, the coulombic efficiency of the first cycle was dependent strongly on the content of Na^+ [37]. To improve the initial Na content, Wang et.al. $Na_{1.72}$Mn $Fe(CN)_6$ with higher Na content was prepared with a higher Na^+ content in the water solution to obtain an initial charge and discharge capacities of 143 and 134 mAh g^{-1}, respectively [53].

In order to enhance the capacity of PB/PBAs, a series of PB/PBAs have been synthesized with the unique dual electron redox couples in which N ligand sites are substituted by electrochemically active transition metal. For example, Takachi et al. [54] synthesized $Na_{1.6}Co[Fe(CN)_6]_{0.9}\cdot 2.9H_2O$ using electrochemical deposition with $K_3[Fe(CN)_6]$, $Co(NO_3)_2$, and $Na(NO_3)$ as the raw materials. This compound delivered a high capacity of 135 mAh g^{-1} and an average operating voltage of 3.6 V. Liu et al. [37] synthesized a $Na_xFeFe(CN)_6$ by coprecipitation method and obtained a capacity of 120.7 mAh g^{-1} at 200 mA g^{-1}. Bie et al. [55] synthesized a $Na_{1.58}Mn[Fe(CN)_6]_{0.80}\cdot 1.8H_2O$, which had a capacity of 126 mAh g^{-1} at 30 mA g^{-1}. $Na_2MnMn(CN)_6$ was synthesized by Lee et al. [56], which showed a high specific capacity of 209 mAh g^{-1} in a propylene carbonate electrolyte.

Due to the existence of crystal water in PB/PBAs, some side reactions could occur during Na^+ intercalation process, resulting in the increase of cathode impedance and the irreversible capacity loss [57]. For example,

Table 1
The performance of representative PBAs materials in sodium-ion batteries.

PBAs	Electrolytes	Voltage range (V)	Capacity[a]	Rate capacity[b]	Cycling stability[c]	Ref.
Na-MnHCFe	1 M $NaPF_6$/EC-DEC	2–4.2 vs. Na^+/Na	126/30 mA g^{-1}	–	60%/50/30 mA g^{-1}	[55]
$Na_{1.87}Ni_{0.05}Mn_{0.95}[Fe(CN)_6]_{0.98}\square_{0.02}\cdot 4.06H_2O$	1 M $NaPF_6$/EC-DEC	2–4.0 vs. Na^+/Na	120/50 mA g^{-1}	97/800 mA g^{-1}	91.6%/400/100 mA g^{-1}	[36]
$Fe_4[Fe(CN)_6]_3$	1 M $NaPF_6$/EC-DEC	2.0–4.2 vs. Na^+/Na	115.2/50 mA g^{-1}	33.9/800 mA g^{-1}	86.6%/200/50 mA g^{-1}	[102]
$Na_{0.99}Mn_{0.37}Fe_{0.63}[Fe(CN)_6]_{0.96}\cdot\square_{0.04}\cdot 1.36H_2O$	0.8 M $NaPF_6$/EC-DMC	2.0–4 vs. Na^+/Na	117.3/1 C	111.5/5 C	98.5%/200/1 C	[70]
$Na_{1.02}Fe[Fe(CN)_6]_{0.95}\square_{0.05}$	–	2.0–4.0 vs. Na^+/Na	140/0.1 C	51/10 C	95.8%/500/1 C	[69]
HCS-PBMN	1 M $NaPF_6$/EC-DEC	2.0–4.2 vs. Na^+/Na	123/50 mA g^{-1}	52/3200 mA g^{-1}	82.3%/600/50 mA g^{-1}	[68]
PB@C	1 M $NaPF_6$/EC-DEC	2.0–4 vs. Na^+/Na	120/100 mA g^{-1}	77.5/90 C	90%/2000/20 C	[71]
$Na_{1.56}Fe[Fe(CN)_6]\cdot 3.1H_2O$	1 M $NaClO_4$/EC-DEC	2.0–4 vs. Na^+/Na	103.6/20 mA g^{-1}	–	97%/400/20 mA g^{-1}	[58]
NMHFC@PPy	1 M $NaClO_4$/EC-DEC	2.0–4.2 vs. Na^+/Na	124/0.1 C	55.6/40 C	61.3%/200/2 C	[74]
$Na_{1.70}FeFe(CN)_6$	1 M $NaClO_4$/ PC-EC	2.0–4.2 vs. Na^+/Na	120.7/ 200 mA g^{-1}	73.6/ 1200 mA g^{-1}	75.3%/100/200 mA g^{-1}	[37]
$FeFe(CN)_6$/carbon cloth	1 M $NaClO_4$/ PC-EC	2.0–4 vs. Na^+/Na	82/0.2 C	62/ 5 C	81.2%/1000/1 C	[77]
HC-PB/GO	1 M $NaClO_4$/EC-DEC	2.0–4.2 vs. Na^+/Na	150/25 mA g^{-1}	135/500 mA g^{-1}	80.6%/50/25 mA g^{-1}	[63]
$K_{0.33}FeFe(CN)_6$/RGO	1 M $NaClO_4$/EC-DEC	2.0–3.8 vs. Na^+/Na	159/0.5 C	126/20 C	90.1%/500/10 C	[75]
$Na_2CoFe(CN)_6$	1 M $NaClO_4$/EC-DEC	2.0–4.1 vs. Na^+/Na	153/10 mA g^{-1}	60/500 mA g^{-1}	90%/200/100 mA g^{-1}	[31]
$Na_2Ni_{0.39}Co_{0.61}Fe(CN)_6$	1 M $NaPF_6$/EC-DEC	2.0–4.2 vs. Na^+/Na	90/50 mA g^{-1}	74/800 mA g^{-1}	88.9%/100/50 mA g^{-1}	[65]
HQ-NaFe	1 M $NaPF_6$/EC-DEC	2.0–4 vs. (Na^+/Na)	170/25 mA g^{-1}	70/600 mA g^{-1}	100%/150/25 mA g^{-1}	[29]
V/Fe PBA	0.5 m Na_2SO_4 + 5 m H_2SO_4	0.45–1.15 vs. Ag/AgCl	91/110 mA g^{-1}	54/3520 mA g^{-1}	79%/250/1760 mA g^{-1}	[100]
NiHCF	6 M $NaClO_4$	0–1 vs. Ag/AgCl	68.1/0.5 C	63.1/10 C	96.3%/1000/10 C	[95]
$Na_2Cu_{0.6}Ni_{0.4}[Fe(CN)_6]$	6 M $NaClO_4$	0–1 vs. Ag/AgCl	62.5/0.5 C	56/10 C	96%/1000/10 C	[94]
$Na_{1.24}Mn[Fe(CN)_6]_{0.81}\cdot 1.28H_2O$	17 M $NaClO_4$	0–1.3 vs. Ag/AgCl	116/ 2.0 mA cm^{-2}	–	92/100/5.0 mA cm^{-2}	[96]
$Na_2VO_x[Fe(CN)_6]$	3 M $NaNO_3$ + 3.6 M H_2SO_4	0.45–1.2 vs. Ag/AgCl	79/30 C	–	–	[87]
CuHCF	saturated $NaNO_3$	0–1.1 (vs. SCE)	100/300 mA g^{-1}	58/20 C	80%/250/300 mA g^{-1}	[93]
NFF-N0.23	1 M $NaNO_3$	-0.2–1.2 (vs. SCE)	105.9/ 200 mA g^{-1}	55.5/ 2000 mA g^{-1}	73.1%/1000/ 1000 mA g^{-1}	[98]
$Na_{1.85}Co[Fe(CN)_6]_{0.99}\cdot 2.5H_2O$	1 M $NaSO_4$	0–1 vs. Ag/AgCl	128/130 mAh g^{-1}	61/20 C	89.2%/800/5 C	[33]

[a] Capacity: initial specific capacity at specific current density (mAh g^{-1} or mAh cm^{-1}/mA g^{-1} or C). The default is mAh g^{-1} when the unit is not marked.
[b] Rate capacity: specific capacity at maximum current density (mAh g^{-1} or mAh cm^{-1}/mA g^{-1} or C). The default is mAh g^{-1} when the unit is not marked.
[c] Cycling stability: retention ratio of capacity after some cycles of charge and discharge at a specific rate (%/cycles/mA g^{-1} or C).

Chou et al. [58] found that adding NaCl to the precursor solution could increase the Na^+ content in PB/PBAs, and the more Na-ion was inserted, the less vacancy and coordination water were formed. This Na^+ addition could not only enhance the cycling stability due to the reduction of vacancy and coordination water, but also improve the specific capacity. Mössbauer spectra and TGA results shown in Fig. 5a confirm that the introduction of more Na^+ into the $Na_{1+x}Fe[Fe(CN)_6]$ framework can reduce the amount of vacancy and coordination water per unit cell, making improvement of the structure and the electrochemical performance.

Hu et al. [59] synthesized monodisperse coordination polymer nanoparticles by adding chelating agents. The experimental results showed that the introduction of sodium citrate in the reaction could slow down the crystallization process of PBAs, which was beneficial to improving the crystallinity of the material. For example, Wu et al. [31] synthesized $Na_2CoFe(CN)_6$ nanocrystals with high quality and free vacancy using such a kinetically controlled crystallization.

The synthesis of traditional PBAs is usually carried out by the co-precipitation reaction of transition metal cation and $[Fe(CN)_6]^{4-}$/$[Fe(CN)_6]^{3-}$. During the process of co-precipitation, the rapid formation of crystal nuclei and fast lattice growth unavoidably lead to a large number of lattice defects and $Fe(CN)_6$ vacancy in PBA crystal. In the synthetic route shown in Fig. 5b, Co^{2+} ion coordinates with citric acid to form Co-citric acid chelate. Due to the strong complex ability of Co^{2+} chelate, Co^{2+} is released slowly in the solution and then coprecipitated with hexacyanoferrate ions, which the introduction of citric acid greatly slows down the whole nucleation process and effectively inhibits the generation of vacancy [31,33]. Compared to conventional co-precipitation, citric acid inhibitor assisted precipitation could reduce the number of $Fe(CN)_6$ defects from 12% to 1%. Attributed to the high crystallinity and low defects through this method as well as two-electron transfer derived from the redox center of Co^{2+}/Co^{3+} and Fe^{2+}/Fe^{3+}, the prepared $Na_2CoFe(CN)_6$ material showed a highly reversible reaction of 1.85 Na^+ per unit with a high capacity of 150 mAh g^{-1} and 90% of capacity retention after 200 cycles. Moreover, You et al. [60] proved that $Na_{1.63}Fe_{1.89}(CN)_6$ with high Na^+ content could be obtained in the presence of ascorbic acid or in the nitrogen atmosphere, which showed a high initial coulombic efficiency. When ascorbic acid and N_2 are applied together, the oxidation of $Fe^{2+}/[Fe^{II}(CN)_6]^{4-}$ could be effectively inhibited, and the Na^+ content could reach to 1.63 per unit. This Na^+-riched material showed a high coulombic efficiency (~98%) in the first cycle, followed by a high coulombic efficiency (~100%) with a high specific capacity of 150 mAh g^{-1} and high capacity retention (90% after 200 cycles).

The drying process can also affect the crystal water content in the crystal lattice. PBAs dried in vacuum can further remove the crystal water content. Song et al. [61] compared the effects of air drying and vacuum drying on the electrochemical performance of $Na_2MnFe(CN)_6\cdot zH_2O$ and revealed the structural changes of the material during the Na^+ insertion. After vacuum drying at 100 °C for 30 h, the voltages of $Na_2Mn[Fe(CN)_6]$ were 3.53 V and 3.44 V respectively on the charging and discharging platforms with a reversible capacity of 150 mAh g^{-1} at 0.1 C. XRD analysis showed that $Na_2Mn[Fe(CN)_6]$ with different crystal water contents could have different structures, indicating that the adding of interstitial water could transform the rhombohedral structure into a monocline structure. As shown in Fig. 5c, this reversible phase transition can be demonstrated in Na^+ extraction/insertion, and the mixed intermediate phase combining the rhombohedral phase with monoclinic phase is discovered in this process.

Micro-cubic PB without coordination water was synthesized by Yang et al. [62] through electron exchange during the heat-treatment of a graphene oxide-PB composite (Fig. 5d). During the co-heating process, the oxide group of GO can obtain an electron from Fe^{2+} site of $Fe2^{2+}(NC)_5(OH_2)$ in $Na_{0.81}Fe[Fe(CN)_6]_{0.79}\square_{0.21}$ and then departs from

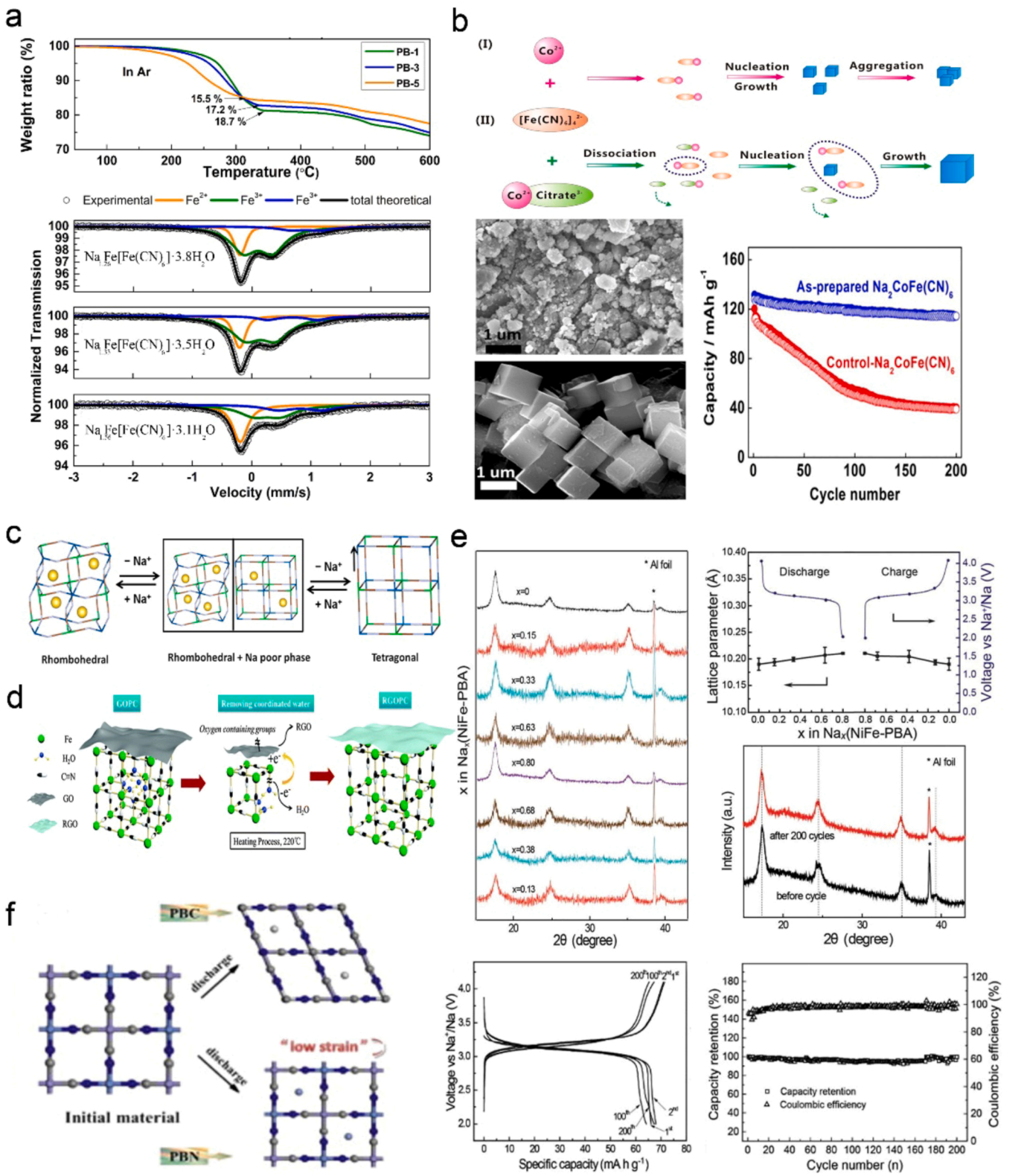

Fig. 5. (a) TGA and Mössbauer spectra and cycling performance of $Na_{1+x}Fe[Fe(CN)_6]$ powder samples. PB-1, PB-3, and PB-5 represent $Na_{1.26}Fe[Fe(CN)_6]\cdot 3.8H_2O$, $Na_{1.33}Fe[Fe(CN)_6]\cdot 3.5H_2O$, and $Na_{1.56}Fe[Fe(CN)_6]\cdot 3.1H_2O$, respectively. Reprinted with permission [58]. Copyright 2015, American Chemical Society. (b) Schematic illustration of the conventional coprecipitation method (I) and the citrate-assisted controlled crystallization process (II) for the synthesis of $Na_2CoFe(CN)_6$ and their SEM images and performance comparison. Reprinted with permission [31]. Copyright 2016, American Chemical Society. (c) Schematic illustration of the structural evolution of R-$Na_{2-\delta}$MnHCF along with Na^+ extraction and insertion. Reprinted with permission [61]. Copyright 2015, American Chemical Society. (d) A schematic mechanism for the removal of coordinated water from RGOPC and their performance with different GO contents. Reprinted with permission [62]. Copyright 2015, The Royal Society of Chemistry. (e) Ex-situ XRD patterns and electrochemical characterization of NiFe-PBA cathodes. Reprinted with permission [64]. Copyright 2013, The Royal Society of Chemistry. (f) Schematic of the crystal structure change of PBN and PBC during discharge. Reprinted with permission [65]. Copyright 2015 Elsevier.

GO to compensate for the electrical change of $Fe2^{2+/3+}$ in the PB frame, and (OH_2) is removed from $Fe^{2+}(NC)_5(OH_2)$ to form a cation vacancy. Based on these principles, coordinated water is released from the vacancy during electron exchange. The results showed that graphene oxide-PB composites with 9 wt% GO has a high specific capacity of 163.3 mAh g^{-1} at a current density of 30 mA g^{-1}. Prabakar et al. [63] took Fe_2O_3 as the Fe^{3+} source and bound it tightly to GO (Fe_2O_3/GO). Fe^{3+} was released from Fe_2O_3 through reacting with a hydrochloric acid solution containing $Fe(CN)_6^{4-}$, which promoted the formation of HC-PB on GO. This HC-PB/GO composite showed a low [$Fe(CN)_6$] vacancy. When used as the cathode for SIBs, its rate performance could reach to 192 mWh g^{-1} at 5000 mA g^{-1}.

Another issue to be solved is the lattice distortion. During the cycling of SIBs, the Na ions can repeatedly intercalate and deintercalate, which tends to change the structure. The solutions to the issue are usually divided into two aspects: (1) seeking for zero-strain insertion electrode material; (2) PB/PBAs with special nanostructure to alleviate the stress change of Na^+ during intercalation/deintercalation.

You et al. [64] stabilized the structure by introducing nickel element and explore the mechanism of Na^+ intercalation/deintercalation through X-ray diffraction (XRD). The XRD showed that the lattice parameters of this NiFe-PBA changed slightly during the insertion of Na^+ with a maximum isotropic lattice strain of 0.29% (Fig. 5e), manifesting that, the introduction of nickel element into the structure can effectively adapt to the volume change during charge/discharge process.

Although nickel can stabilize the structure, but nickel is an electrochemical inert element which supplies no contribution on the capacity. Therefore, to enhance capacity, electrochemical active metal elements are usually introduced into the materials to form PB in ternary form. Fig. 5f shows the lattice change of PB containing Co (PBC) and PB containing Ni (PBN) during Na^+ insertion. The former can provide more active sites and higher specific capacity, but the volume can change largely and the cycling stability is poor, while the latter has stable circulation but low specific capacity. Combining the advantages of both, Xie et al. [65] combined the merit of two metal ions and formulated ternary PBAs with Ni, Co, and Fe, in which Ni was used as the framework support, and the Co^{2+}/Co^{3+} and $Fe(CN)_6^{4-/3-}$ as the redox couples providing active sites for the electron to transfer. When Ni and Co replaced N coordination transition metal by 40% and 60% respectively, the initial discharge capacity of the material could be 91 mAh g^{-1}. After 100 cycles at 50 mA g^{-1}, the capacity retention rate was 85.9%, showing a good cycling stability. Similarly, Chen et al. [36] synthesized a $Na_{1.87}Ni_{0.05}Mn_{0.95}$ $[Fe(CN)_6]_{0.98}\square_{0.02}\cdot 4.06H_2O$ with low defect and high crystallization by combining the chemical inhibitors assisted synthesis and the introduction of electrochemical inert (Ni) and active element (Mn).

In order to further optimize the electrochemical performance of PB/PBAs-based sodium-ion batteries, various optimization strategies for structure and morphology have been developed [18]. Suitable structural optimization can shorten the intercalation path of Na^+. Currently, mesocrystalline structure [66], nanostructure [36,67] and core-shell structure [68,69], and hierarchical hollow rod shape have been reported [70]. For example, Feng et al. [70] took MnO_2 as a self-sacrificial template and Mn source to synthesize a hierarchical hollow rod-shaped $Na_{0.99}Mn_{0.37}Fe_{0.63}$ [$Fe(CN)_6$] through a solvent thermal reaction. After 200 cycles at 1 C, this material could give both the high discharge capacity of 117.3 mAh g^{-1} and capacity retention rate of 98.5%, and the specific capacity of 111.5 mAh g^{-1} at 5 C was also achieved with a coulombic efficiency of 93.8%. Hu et al. [69] synthesized a $Na_{1.02}Fe[Fe(CN)_6]_{0.95}\square_{0.05}$ with the yolk-shell structure free of a template method. The hierarchical structure of PB yolk-shell nanoparticles had large specific surface area and short ion transport channel. This cathode material could deliver high discharge capacity (0.1 C, 140 mAh g^{-1}), high rate performance (10 C, 51 mAh g^{-1}), and good cycling stability.

In addition, suitable substrate materials and carbon coating can greatly improve the conductive performance and cycling stability of PB/PBAs. Currently, carbon [71], carbon nanotubes [72], PPy [73,74], graphene [75,76], carbon cloth [77], etc. have been adopted. For example, Yu et al. [76] synthesized $Na_{1.83}Ni_{0.12}Mn_{0.88}Fe(CN)_6$/rGO (denoted as NNM HCF/rGO) nanocomposites with a rich Na^+ content by PVP assisted one-step solution coprecipitation. As the cathode of the SIBs, this NNM HCF/rGO showed the initial charging and discharging capacities of 126/120 mAh g^{-1} at a current density of 20 mA g^{-1}, and the capacity remained 116 mAh g^{-1} after 1100 cycles, indicating the excellent cycling stability. At a high current density of 1000 mA g^{-1}, the capacity still retained a capacity of 86 mAh g^{-1}. Tang et al. [73] synthesized Fe-HCF@PPy cubic microcrystals. The PPy coated on the surface of Fe-HCF could not only act as an electric conductor to enhance the conductivity but also serve as a protective layer to prevent side reactions and structural collapse during the intercalation.

3.1.1.2. PB/PBAs cathodes in aqueous sodium-ion batteries. Compared with organic SIBs, aqueous sodium-ion batteries (ASIBs) can solve the safety issue of highly toxic and flammable organic electrolytes. Although the mechanism of energy storage is similar as that of non-aqueous SIBs, the electrochemical reaction of Na^+ extraction/insertion in the aqueous electrolyte is relatively complex. Therefore, the following principles should be taken into consideration in the selection of positive electrode materials [78,79]: (1) the potential of the Na^+ insertion reaction should be lower than that of the oxygen evolution potential of water in the aqueous environment. When the potential is higher than that of the oxygen evolution potential of water, H_2O will generate O_2 by electrolysis, and the generated oxygen molecules would consume the charges, leading to the low coulombic efficiency; (2) the material should have both high electric conductivity and ionic conductivity, which can exhibit the high-speed ion transfer of the aqueous electrolyte to a certain extent; (3) the material should have high reversible capacity; (4) it should contain diffusion channels that are favor of Na^+ transfer; (5) it is not prone to produce side reactions with H_2O or residual O_2.

In recent years, various ASIBs cathode materials have been developed. At present, the cathode materials are mainly divided into metal oxides (Mn_5O_8 [80], $Na_4Mn_9O_{18}$ [81], and $Na_{0.66}[Mn_{0.66}Ti_{0.34}]O_2$ [82]), polyanionic compounds (nasicon-type $Na_3V_2(PO_4)_3$ [83], $Na_3V_2O_2(PO_4)_2$ [84], and $Na_3MnTi(PO_4)_3$ [85]), PBAs ($Na_2CoFe(CN)_6$ [33], $Na_{1.33}Fe[Fe(CN)_6]_{0.82}$ [86], and $Na_2VO_x[Fe(CN)_6]$ [87]) and organic polymers (poly(2,2,6,6-tetramethylpiperidinyloxy-4-yl vinylether) [88].

The redox potentials of most PBAs are within the range of stable electrochemical window of water, so PBAs are a kind of suitable electrode materials for aqueous batteries. Meanwhile, PBAs have an open three-dimensional frame, which also makes it displayed unique advantages in aqueous system sodium-ion batteries.

Wessells et al. [89] synthesized a $K_{0.6}Ni_{1.2}Fe(CN)_6\cdot 3.6H_2O$ (NiHCF) by chemical coprecipitation. This NiHCF material was tested in a 1 M $NaNO_3$ electrolyte which is acidified pH= 2 with dilute nitric acid. At the operating voltage of 0.59 V vs. SHE, this material showed a specific capacity of ~60 mAh g^{-1} at 0.83 C. At a current density of 41.7 C, it could still maintain 67% of the maximum capacity. At 8.3 C, this material showed insignificant capacity loss after 5000 cycles. Wu et al. [90] used $Na_2NiFe(CN)_6$ as a cathode material and $NaTi_2(PO4)_3$ as an anode to establish a sodium-ion battery. The average output voltage of this battery was 1.27 V with an energy density of 42.5 Wh kg^{-1} and the specific capacity close to 100 mAh g^{-1}. From 1–10 C, the discharge capacity was decayed from 100 mAh g^{-1} to 86 mAh g^{-1}, showing high rate performance. In addition, the sodium-ion battery operated well at 5 C, achieving 79 mAh g^{-1}(88% of the initial capacity) after 250 cycles. There was still more than 70% of the capacity retained at a current density of 10 C. In summary, this NiHCF material could operate in safe with inexpensive aqueous electrolyte and have superior rate performance, energy efficiency and cycle life.

Besides NiHCF, CuHCF has also attracted attention for its high output

potential [91]. Wu et al. [92] synthesized a Na^+-rich hexacyanoferrate (II) ($Na_2CuFe(CN)_6$ as a high-potential cathode, and assembled the ASIBs using $NaTi_2(PO_4)_3$ as a sodium-deficient anode. The battery had an average discharge voltage of 1.4 V and a specific energy of 48 Wh kg^{-1} calculated by the total weight of the electrode active material. The battery went from the initial 100 mAh g^{-1} to 97 mAh g^{-1} in 100 cycles at 2 C, corresponding to a 97% capacity retention rate. At 10 C, the reversible capacity was decreased slightly to 85 mAh g^{-1}, then slowly decayed to 74 mAh g^{-1} up to the 1000 th cycle, maintaining a high capacity retention of 88%. When the power density was 91 W kg^{-1}, the specific energy of the battery is 48 Wh kg^{-1}. At a maximum power of 3500 W kg^{-1}, the specific energy density of this battery was still at 16.6 Wh kg^{-1}. Combining the advantages of the high working voltage of CuHCF and the low working voltage of Fe^{2+}/Fe^{3+} in FeHCF, Wang et al. [93] constructed an all-PB-based aqueous sodium-ion battery with CuHCF as the cathode material and FeHCF as the anode material. The obtained battery could deliver an average working voltage of 0.70 V and a reversible capacity of 50 mAh g^{-1} at 5 C. After 250 cycles, the battery could maintain 86% of its initial capacity. In order to obtain the copper hexacyanate cathode with high working potential and long cycling stability, Li et al. [94] introduced nickel into copper hexacyanoferrate to form nickel copper alloy hexacyanoferrates, which provided a high operating potential and an excellent cycling performance.

Furthermore , a high concentration of electrolyte was utilized to inhibit the side reaction between electrode and electrolyte, so as to improve the electrochemical performance [95,96]. Based on the single-electron reaction mechanism of $Fe^{3+}/^{2+}$ redox couple, $Na_2Cu_{0.6}Ni_{0.4}[Fe(CN)_6]$ was reported with a reversible capacity of 62 mAh g^{-1} at potential of 0.62 V vs. Ag/AgCl. Even at a high current density of 10 C, its discharge capacity after 1000 cycles could still maintain 56 mAh g^{-1} with a capacity retention of 96%. Nakamoto et al. [97] used $Na_{1.24}Mn[Fe(CN)_6]_{0.81}\bullet 1.28H_2O$ as a cathode material and $K_{0.01}Mn[Cr(CN)_6]_{0.72}\bullet 2.01H_2O$ as the anode one to establish an ASIB with 17 M $NaClO_4$ electrolyte, which could realize an over 2 V operational voltage for high energy density.

Since the electrochemical process of the above material is a single electron reaction mechanism, which is limited by the theoretical specific capacity and cannot provide a high energy density, the researchers have also developed PBAs with two-electron transfer, such as $Na_xM[Fe(CN)_6]$ (M=Fe, Co, Mn, etc.) to improve the overall electrochemical performance the electrode material. For instance, when M=Fe, the two-electron transfer process can be described by the following reaction equation: $Na_xFe^{II}Fe^{II}(CN)_6 \leftrightarrow Na^+ + Na_{x-1}Fe^{III}Fe^{II}(CN)_6 + e^- \leftrightarrow 2Na^+ + Na_{x-2}Fe^{III}Fe^{III}(CN)_6 + 2e^-$.

Wu et al. [31] synthesized $Na_2CoFe(CN)_6$ nanocrystals with low defects and high crystallization by citrate assisted crystallization control method. Due to its high crystallinity and inhibition of $Fe(CN)_6$ defects, the obtained $Na_2CoFe(CN)_6$ material showed a highly reversible 2-Na reaction, a high capacity of 150 mAh g^{-1}, and a 90% long cycle capacity in more than 200 cycles.

A series of low-cost nickel-substituted $Na_xFeFe(CN)_6$ (NFF-N_x) cathode nanocrystals were developed by Wang et al. [98] through citric acid assisted coprecipitation under nitrogen atmosphere, and their electrochemical performances in ASIBs were studied. Their results showed that the electrochemical performance of the $Na_xFeFe(CN)_6$ with 23% Ni^{2+} was the best. The NFF-$N_{0.23}$ exhibited a high discharge capacity of 105.9 mAh g^{-1} at 200 mA $g^{-1}$and excellent cycling stability of capacity 73.1% capacity retention up to 1000 cycles at 1000 mA g^{-1}. Even at the high rate of 2000 mA g^{-1}, the reversible capacity could still be 55.5 mAh g^{-1}. Replacing partial high spin Fe^{2+} with Ni^{2+} could not only enhance the phase stability but also improve the conductivity of the cathode material, enabling it to possess high rate performance.

Pasta et al. [99] studied the electrochemical and structural properties of manganese hexacyanoferrates (MnHCFe), cobalt hexacyanoferrates (CoHCFe), and their mixtures. The results showed that CoHCFe had better electrochemical reversibility, while MnHCFe possessed a higher insertion potential and low cost. However, both still suffered the lattice expansion as well as the competition with the oxidation of water to oxygen during charge/discharge process. However, further studies showed that the single-phase mixtures of them could not combine both advantage to greatly enhance their performance, instead, they exhibited poor performance and the irreversibility, which was attributed to the oxidation of the aqueous electrolyte and the serious phase instability of the manganese-containing mixture. They studied the contribution to specific capacity of each redox couple, relative performance, and stability, and also established the direct relationship among the crystallography, electronic states, electrochemical reversibility, and kinetics.

In addition to the common PBAs based on the above transition metal elements, Lee et al. [100] synthesized $V_3[Fe(CN)_6]_2$ through a simple chemical coprecipitation. V ions exhibited a variety of oxidation states of + 2~+ 5. Under the condition that the aqueous electrolyte remained stable, both V and Fe ions were expected to effectively participate in the multi-electron energy storage process. Moreover, V ion has the lightest atomic weight among the transition metal ions tin PBAs, which is beneficial to increasing the gravimetric energy and power densities. At a current density of 110 mA g^{-1}(rate of 1.2 C), a V/Fe-based PBA showed a capacity of 91 mAh g^{-1}. At a high rate of 3520 mA g^{-1}, this material could deliver a high discharge capacity of 54 mAh g^{-1}. Xie et al. [101] synthesized $Na_{0.66}Ti\ [Fe(CN)_6]_{0.92}\square 0.08$ with $Ti^{3+}/^{4+}$ and $[Fe(CN)6]^{4-/3-}$ redox couples by substituting titanium for the position of transition metal. The reversible capacity of 92.3 mAh g^{-1} was obtained.

There are many researches on PB/PBAs for sodium-ion batteries, and a large number of studies have proved that PB/PBAs have high electrochemical performance for electrical energy storage devices. Moreover, the PB/PBAs which are composed of low-cost and environmentally-friendly elements such as Mn and Fe with highly safe water-electrolyte systems can provide favorable conditions for many applications. If the phase change of Mn-containing PBAs and the electrode dissolution in the electrolyte can be solved in the future, its application in large-scale energy storage is foreseeable.

3.1.2. PB/PBAs cathodes in potassium-ion batteries

The main advantages of PIBs are as follows [103]: (1) abundant potassium resources decrease the cost of batteries; (2) PIB has high operating voltage because the standard redox potential of K^+/K is − 2.93 V vs. SHE is close to the standard redox potential of Li^+/Li (−3.04 V vs. SHE); (3) the solvated K^+ has a smaller stoke radius due to its weak Lewis acidity as well as a low interface reaction resistance due to the small desolvation activation energy and high ion transfer number/ion conductivity, contributing to better kinetics and rate performance; (4) low-cost Al foil can be used as both the current collector of anode and cathode in PIBs because K^+ does not form an electrochemical alloy with Al.

Although PIBs have many advantages, they also face several challenges: (1) larger ion radius and heavier atomic mass limit the theoretical capacity to some extent; (2) during the process of potassium intercalation and deintercalation, the material structure is prone to be deformed severely and the capacity will decline faster. Thus, similar to SIBs, one of the major tasks is to identify a suitable cathode to reversibly insert a large-size K-ion [104]. The structural stability and high theoretical capacity of PB/PBAs make it possible to develop efficient PIBs. Some representative PB/PBAs reported in PIBs are summarized in Table 3.

3.1.2.1. PB/PBAs cathodes for non-aqueous potassium-ion batteries. Since 2004, Eftekhari [105] discovered that $K_2Fe[Fe(CN)_6]$ could reversibly store K^+ in a non-aqueous electrolyte (1 M KBF_4 in 3:7 EC/EMC) and the chemical diffusion coefficient of K^+ in the battery was higher than that of Li^+ in the LIBs. After that, the PB/PBAs had been proven several times to be successfully applied in non-aqueous PIBs.

Table 2
Ionic Radius (Unit: pm) and Relative Energies (Unit: eV) of $AFe[Fe(CN)_6]$ and $AEFe[Fe(CN)_6]$ (A, Alkali; AE, Alkaline Earth) with A^+ or AE^{2+} occupying Different Interstitial Sites. (Adapted with permission [106]. Copyright 2013, American Chemical Society).

	Li	Na	K	Rb	Cs	Mg	Ca	Sr	Ba
radius	90	116	152	166	181	86	114	132	149
8c	0.979	0.405	0	0	0	3.391	3.403	2.316	1.848
24d	0.062	0	0.778	1.420	2.184	0	0	0	0.595
32f	0.361	0.132	0.103	0.265	0.376	0.608	0.700	0.057	0
32f	0.717	0.222	0.118	0.269	0.466	1.134	0.869	0.295	0.083
48g	0	0.077	0.061	0.064	0.056	0.124	0.117	0.173	0.078

Table 3
The performance of representative PBAs materials in potassium-ion batteries.

PBAs	Electrolytes	Voltage Range (V)	Capacity	Rate capacity	Cycling stability	Ref.
$KFe^{II}[Fe^{III}(CN)_6]$	1 M KPF_6/EC-DEC-PC	2–4.5 vs. K^+/K	118.7/10 mA g^{-1}	40.6/500 mA g^{-1}	93.73%/100/ 10 mA g^{-1}	[103]
FCC@KPB	1 M KPF_6/PC+ 10 vol% FEC	2–3.8 vs. K^+/K	0.110/ 0.02 mA cm^{-2}	0.026 mAh cm^{-2}/ 0.3 mA cm^{-2}	87%/100/ 0.1 mA cm^{-2}	[108]
$K_{1.69}Fe[Fe(CN)_6]_{0.90}{\cdot}0.4H_2O$	0.5 M KPF_6/EC-DEC+ 5% FEC	2–4.4 vs. K^+/K	140/10 mA g^{-1}	120/100 mA g^{-1}	65%/300/ 100 mA g^{-1}	[104]
$PB@MoS_2$	0.5 M K_2SO_4	-0.5–1 vs. Ag/ AgCl	215/1 A g^{-1}	–	97%/10 000/ 10 A g^{-1}	[110]
$K_{1.89}Mn[Fe(CN)_6]_{0.92}$	Saturated $KClO_4$/PC+ 10 wt % FEC	2.5–4.6 vs. K^+/K	142.4/0.2 C	–	–	[107]
RGO@PB@SSM	0.8 M KPF_6 /EC-DEC+ 5% FEC	2.2–4 vs. K^+/K	96.8/10 mA g^{-1}	35/1000 mA g^{-1}	75.1%/305/ 50 mA g^{-1}	[109]
$K_{1.85}Fe_{0.33}Mn_{0.67}[Fe(CN)_6]_{0.98}{\cdot}0.77H_2O$	22 M KCF_3SO_3	0–1.2 vs. Ag/ AgCl	135/0.5 C	94/100 C	90%/ 10,000/100 C	[111]
$K_2NiFe(CN)_6{\cdot}1.2H_2O$	1 m KNO_3 + 0.01 M HNO3	0–1 vs. SCE	77.4/ 5 C	53.8/200 C	100%/100/200 C	[112]
$K_2Fe^{II}[Fe^{II}(CN)_6]{\cdot}2H_2O$	0.5 K_2SO_4	0–1.2 vs. Ag/ AgCl	120/4 C	93/21.4 C	85% /500/21.4 C	[113]
$K_{0.71}Cu[Fe(CN)_6]_{0.72}{\cdot}3.7H_2O$	1 M KNO_3 + 0.01 M HNO_3	0.8–1.2 vs. SHE	59.14/0.83 C	40.1/83 C	83%/ 40,000/17 C	[91]

It is noticed that the relative stability of the interstitial site of PBAs is closely related to the ion radius of the inserted cation. Among the possible interstitial sites in the FeHCF cubic structure (Fig. 6a), the face-centered 24 d site can provide the minimum free space, while the body-centered 8c site with the body as the center can provide the maximum free space. Through the first-principles calculation (GGA+*U*), Ling et al. [106] proved that K^+ was generally more inclined to occupy the body center of the empty cube, and as shown in Table 2, K^+ has lower insertion energy than those of Li^+ and Na^+. Therefore, the material structure is relatively stable during the intercalation and deintercalation of K^+. Compared with Li^+, the insertion of K^+ occurs at a higher voltage, which manifests that a higher energy density can be obtained.

Chong et al. [103] synthesized $KFe^{II}[Fe^{III}(CN)_6]$ (KFFCN) and used it as the cathode material for non-aqueous PIBs. This material showed a

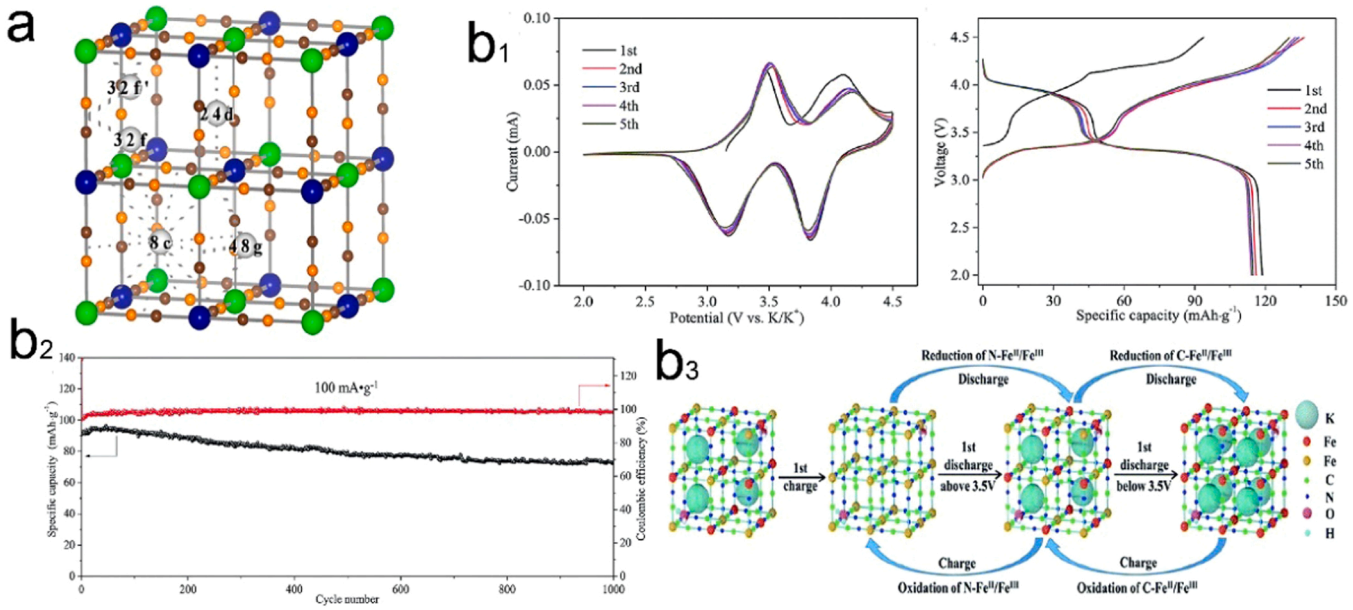

Fig. 6. (a) Crystal structure of iron hexacyanoferrate ($Fe[Fe(CN)_6]$) and possible interstitial sites. Reprinted with permission [106]. Copyright 2013, American Chemical Society. (b) CV profiles (b1), cycling performance (b2), and schematic view of the K^+ extraction/insertion mechanism during the initial charge-discharge processes and subsequent cycles for the KFFCN electrode (b3). Reprinted with permission [103]. Copyright 2017, The Royal Society of Chemistry.

high reversibility during CV test and delivered a discharge capacity of 118.7 mAh g^{-1} at 10 mA g^{-1} (Fig. 6b_1). It could give an ultra-long cycling life of 1000 cycles at 100 mA g^{-1}, and the corresponding capacity attenuation rate of each cycle was only 0.195% (Fig. 6b_2). In order to find out the reason for the high electrochemical performance of this material, the intercalation/deintercalation mechanism was studied by ex-situ characterizations. The electrochemical K^+ storage of this KFFCN was found to depend on the redox of Fe^{II}/Fe^{III} and the intercalation/deintercalation of K^+ were carried out through the solid solution process (Fig. 6b_3). During the whole process, it maintained the cubic structure, which made a clear distinction from the mechanism of simultaneous occurrence of intercalation and phase transformation.

Xue et al. [107] fabricated $K_{1.89}Mn[Fe(CN)_6]_{0.92}{\cdot}0.75H_2O$ by coprecipitation, which could host two K^+. The charge and discharge capacities were found to be 146.2 mAh g^{-1} and 142.4 mAh g^{-1} at 0.2 C, respectively, close to the theoretical capacity of 156 mAh g^{-1}. Fe^{III}/Fe^{II} and Mn^{III}/Mn^{II} redox couples could provide two high voltage flat platform about 3.6 V, and low-cost Mn also gave the material certain competitiveness.

He and Nazar [104] demonstrated the importance of controlling the size of PBAs nanoparticles for cathode materials for PIBs. Several different sizes of KFeHCF (about 20–200 nm) were synthesized and found that $K_{1.7}Fe[Fe(CN)_6]_{0.9}$ with a size of about 20 nm could give a better kinetic and optimal electrochemical performance.,

In recent years, researchers have further improved the electrochemical performance of PBAs for PIBs by changing the substrate materials and compositing them with other materials. For example, Guo et al. [108] obtained FCC@KPB by using carbon cloth derived from cotton cloth as the substrate. Zhu et al. [109] prepared rGO@PB@SSM by combining PB with stainless steel iron mesh and rGO. Morant-Giner et al. [110] compounded PB with molybdenum disulfide to synthesize $K_{0.47}Fe^{III}_4[Fe^{II}(CN)_6]_{3.14}@(MoSO_{1.7})_{0.44}{\cdot}18H_2O$.

3.1.2.2. PB/PBAs cathodes for aqueous potassium-ion batteries. The challenges of aqueous potassium-ion battery (APIBs) are similar to those of ASIBs. The narrow voltage window and the dissolution of electrode material in aqueous electrolyte are still the key factors restricting the development of APIBs. However, compared with ASIBs, APIBs has their unique advantages: (1) the standard electrode potential of potassium is lower than that of sodium, indicating that potassium cathode of the same type structure has higher voltage; and (2) the ionic conductivity of K^+ is usually higher than that of Li^+ and Na^+ in aqueous solution. In general, APIBs is a promising candidate for grid-scale energy storage due to its low-cost and high safety.

Wessells et al. [91] synthesized $K_{0.71}Cu[Fe(CN)_6]_{0.72}{\cdot}3.7H_2O$ by replacing Fe^{3+} with Cu^{2+}, which was coordinated nitrogen in $K_3Fe(CN)_6$, and it was tested in an electrolyte containing 1 M KNO_3/0.01 M HNO_3 (pH=2). The capacity retention was 94.6% after 10,000 cycles at 17 C, and 83% after 40,000 cycles, indicating the long cycling stability of the material. On this basis, they also conducted Cu and Ni co-doping to synthesize a single-phase $Cu_{0.56}Ni_{0.44}HCF$. After 2000 cycles at 500 mA g^{-1} in 1 M KNO_3, the $Cu_{0.56}$ $Ni_{0.44}HCF$ showed a capacity retention of 91%. Ren et al. [112] synthesized a potassium-rich mesoporous nickel ferrocyanide (II) ($K_2NiFe(CN)_6{\cdot}1.2H_2O$) by co-precipitation. This material exhibited a high rate performance and achieved ultra-fast charging and discharging. At 500 C, a single charge/discharge was only 4.1 s with a specific capacity of 42.1 mAh g^{-1}. Su et al. [113] synthesized $K_2Fe^{II}[Fe^{II}(CN)_6]{\cdot}2H_2O$ nanocrystal with uniform particle size distribution by solvent heat method at low temperature. The discharge capacities could reach to 120 mAh g^{-1}, 111 mAh g^{-1} and 109 mAh g^{-1} at 200, 500 and 1000 mA g^{-1}, respectively. Even at a high current density of 300 mA g^{-1}, a capacity of 93 mAh g^{-1} could still be maintained. By means of ex-situ XRD measurements, it was found that all the major diffraction peaks were maintained during the charging and discharging processes, indicating the stability of the crystal structure of this material during the extraction/insertion of K^+.

Jiang et al. [111] used the manganese-rich potassium PB ($K_xFe_yMn_{1-y}[Fe(CN)_6]_w{\cdot}zH_2O$) as a cathode, 3,4,9, 10-perylene tetracarboxylic diimide (PTCDI) as an anode, and 22 M KCF_3SO_3 as the electrolyte to construct APIBs, which showed stable voltage (0–2.6 V), high specific capacity (135 mAh g^{-1} at 0.5 C), wide temperature region (−20 to 60 °C), high power (80 Wh kg^{-1}), and long life-span (73% of the capacity remained after 2000 cycles at 4 C). However, this material had a serious dissolution problem when cycling in the electrolyte with low salt concentration. The authors reported that the dissolution of the electrode was significantly reduced after using a high salt concentration electrolyte of 22 M KCF_3SO_3, but both the voltage and cycling attenuations were still existed. Through ex-situ XRD, ex-situ hard X-ray absorption spectroscopy (hXAS) and first-principles calculations, the improvement of structural and electrochemical properties by substituting iron for manganese could be foreseen. XRD showed that the energy storage mechanism of Fe-substituted MHCF was the solid solution reaction and phase transition between monoclinic and cubic faces. Phase transition was usually caused by the Mn^{3+} Jahn Teller effect of MnN_6 octahedron in the process of charging. The substitution of Fe could reduce Mn^{3+} content and inhibit the phase transition caused by the Jahn-teller effect to some extent. In addition, Fe substitution could change the valence mechanism of Mn^{2+}/Mn^{3+}-N electric couple, making the redox reaction of Mn^{2+}/Mn^{3+}-N asymmetric. Therefore, the material exhibited a better cycling stability. The first-principles calculations proved that after the substitution, KFeMnHCF-3565 had a smaller bandgap and a lower K^+ ion diffusion activation energy, thus enhancing both the electron and K^+ ion conductivities. The authors also inhibited the dissolution of positive and negative materials by increasing the concentration of electrolyte salts to reduce free water.

Wei et al.[114] investigated the electrochemical reaction kinetics and the K^+-ion storage mechanism in $K_2Co[Fe(CN)_6]$ for APIBs through various rates of CV curves. The peak potentials display a small deviation from 2 to 50 mV s^{-1}, manifesting the fast kinetics and low polarization of the $K_2Co[Fe(CN)_6]$ electrode in aqueous electrolytes. The team calculated values b of the equation: $i = av^b$, where i is the current value, a and b are the adjustable values, and v is the scan rate and figured out that the kinetic behavior of $K_2Co[Fe(CN)_6]$ is controlled by a K^+-ion faradaic intercalation process.

Compared with both LIBs and SIBs, the electrochemical performance of PIBs is not outstanding due to its inherent large K^+ radius. However, compared with other positive electrode materials for PIBs, PBAs have shown excellent structural stability and electrochemical performance. In addition, the reversible insertion capability of K^+ in graphite can also provide a possibility for the potential commercial prospect of potassium-ion batteries.

3.2. PB/PBAs cathodes in other low-cost metal-ion batteries

Besides SIBs and PIBs, the researchers have also paid much attention to the multivalent metal-ion batteries. The successful application of PB/PBAs with monovalent metal ions has shifted the focus on their application in multivalent metal-ion batteries. The emergence of such multivalent metal-ion batteries is thought to be a new generation of batteries that could go beyond the monovalent metal-ion batteries. In terms of multivalent metal-ion batteries, the increase of charge density of multivalent cation can increase its electrostatic interaction with the anion, resulting in slow ion transport kinetics during its intercalation/deintercalation processes, thus affecting the electrochemical performance. However, a large number of experiments have also proved that the open three-dimensional ion transport framework of PB/PBAs can meet the requirements of multi-valent metal ion deintercalation. Some representative PB/PBAs materials in multi-metal-ion batteries are summarized in Table 4.

Table 4
The performance of representative PB/PBAs materials in multivalent metal-ion batteries.

PBAs	Electrolytes	Voltage range (V)	Capacity	Rate performance	Cycling	Ref.
Magnesium-ion batteries						
$Mg_{0.27}K_{0.86}Ni[Fe(CN)_6]_{0.954}(H2O)_{0.766}$	0.5 M $Mg(ClO_4)_2$ /AN	–	48.3/0.2 C	–	68.3%/30/0.2 C	[121]
$Na_{1.4}Ni_{1.3}Fe(CN)_6.5H_2O$	1 M $MgSO_4$	-0.2–0.75 vs. Ag/AgCl	65/0.1 A g^{-1}	39/10 A g^{-1}	–	[119]
NFCN	1 M $Mg(TFSI)_2$ /PC	-1–3 vs. a BP2000 carbon anode	40/10 mA g^{-1}	–	–	[120]
CuFe PBA	1 M $Mg(NO_3)_2$	0.1–1.0 vs. Ag/Ag^+	50/0.1 A g^{-1}	37/1 A g^{-1}	–	[118]
Calcium-ion batteries						
CuFe PBA	0.1 M $Ca(CF_3SO_3)_2$/ PC+ 0.6 M H_2O	–	70/0.2 C	–	–	[136]
CuFe PBA	8.4 M $Ca(NO_3)_2$		65/1 C	–	88.6/5000/10 C	[125]
$K_2BaFe(CN)_6$	1 M $Ca(ClO_4)_2$ /AN	–	55.8/ 12.5 mA g^{-1}	–	–	[126]
KNiFe-PBA	0.5 M $Ca(TFSI)_2$ /AN	-1.0–1.0 vs. Ag/Ag^+	45/25 μA cm^{-2}	–	–	[137]
Zinc-ion batteries						
$K_{0.86}Ni[Fe(CN)_6]_{0.954}(H_2O)_{0.766}$	0.5 M $Zn(ClO_4)_2$ /AN	–	55.6/0.2 C	26.8/1 C	–	[128]
$FeFe(CN)_6$	1.0 M $Zn(OAc)_2$/([Ch]OAc+30 wt % H_2O)	0.8–2.0 vs. Zn^{2+}/Zn	120/10 mA g^{-1}	30/60 mA g^{-1}	–	[138]
$K_{0.71}Cu[Fe(CN)_6]_{0.72}·3.7H_2O$	20 mM ZnSO4	–	54/60 mA g^{-1}	43.7/10 C	96.3%/100/ 60 mA g^{-1}	[139]
C-RZnHCF	3 M $ZnSO_4$	–	69.1/60 mA g^{-1}	60.5/ 3000 mA g^{-1}	93.0%/100/ 300 mA g^{-1}	[127]
ZnHCF[a]	1 M $ZnSO_4$	0.8–2.0 vs. Zn^{2+}/Zn	65.4/1 C	32.3/20 C	81%/100/5 C	[140]
Aluminum-ion batteries						
$K_{0.02}Ni_{1.45}[Fe(CN)_6]·2.6H_2O$	5 M $Al(OTf)_3/H_2O$	0.2–1.1 vs. Al^{3+}/Al	46.5/20 mA g^{-1}	–	–	[141]
CuHCF	diglyme: $Al(TFSI)_3$ 5: 1		60/0.1 C	–	5–14/10–15/0.1 C	[129]
$K_2CoFe(CN)_6$	1 M $Al(NO_3)_3$	0–1.2 vs. SCE	50/0.1 A g^{-1}	–	76%/1600/ 0.1 A g^{-1}	[142]

[a] Electrochemical performance in full cell.

3.2.1. PB/PBAs cathodes for magnesium-ion batteries

Magnesium-ion battery stands out among many secondary batteries because of its unique advantages: (1) magnesium has abundant resources and low price; (2) it is highly safe because that it has a high melting point (660 °C) and its stability in the atmosphere is higher than lithium; (3) the light atomic weight of magnesium helps improve the energy density; (4) Mg^{2+} has a small radius (86 pm) and can conduct two-electron redox reaction during cycling so as to deliver a theoretical capacity of 3833 mAh cm^{-1} [115–117].

PB/PBAs have been explored as the cathode materials for rechargeable magnesium-ion batteries in both non-aqueous and aqueous electrolyte systems. For example, Mizuno et al. [118] prepared $K_{0.1}Cu[Fe(CN)_6]_{0.7}·3.6H_2O$ and studied the electrochemical process of Mg^{2+} insertion into PBAs by galvanostatic intermittent titration technique (GITT), X-ray diffraction(XRD), Mössbauer spectroscopy, and X-ray absorption spectroscopy (XAS). This $K_{0.1}Cu[Fe(CN)_6]_{0.7}·3.6H_2O$ was synthesized by using $CuSO_4•5H_2O$ and $K_3Fe(CN)_6$ as the raw materials. For electrochemical testing, 1 M $Mg(NO_3)_2$ and Ag/AgCl in 3 M NaCl were used as the aqueous electrolyte and the reference electrode, respectively. The electrochemical reaction of CuFe-PBA in aqueous electrolyte was expressed as: $xMg^{2+} + 2xe^- + CuFe\ PBA \rightleftarrows Mg_xCuFe\text{-}PBA\ (0 < x < 0.3)$. The reaction mechanism of Mg^{2+} intercalation/deintercalation was carried out in the solid solution state of Mg_x(CuFe-PBA). The divalent cation intercalation can lead to the redoxes of Fe^{III}/Fe^{II} and Cu^{II}/Cu^{I}, which are different from those mechanisms of monovalent cations (Fig. 7a). The specific capacity of CuFe-PBA was 50 mAh g^{-1} (close to the specific capacity of 60 mAh g^{-1}) at 0.1 A g^{-1} and the capacity retention at 1 A g^{-1} was 74%.

Chen et al. [119] used prussian blue type nickel hexacyanoferrate (PBN) $Na_{1.4}Ni_{1.3}Fe(CN)_6.5H_2O$ as the cathode material, polyimide as the anode material and 1 M $MgSO_4$ as the aqueous electrolyte to construct a magnesium-ion battery. As shown in Fig. 7b, the cyclic voltammetry (CV) curves show that Mg^{2+} ions can be inversely extracted from PBN and inserted into polyimide. In the voltage range of 0–1.55 V, this battery could have a capacity retention about 60% after 5000 cycles at 2 A g^{-1}. In addition, this material could withstand the high current density of 10 A g^{-1} maintaining a discharge capacity of 15 mAh g^{-1}.

PBAs can be used not only for aqueous magnesium-ion battery but also for non-aqueous magnesium-ion battery. For example, Lipson et al. [120] synthesized a $Na_{0.45}NiFe(CN)_6$ by co-precipitation with $Ni(NO_3)_2$ and $Na_4Fe(CN)_6$, and proved that it could intercalate Mg^{2+}, Ca^{2+}, and Zn^{2+} effectively, and the initial capacity was 40 mAh g^{-1} in 1 M Mg $(TFSI)_2$ in a PC organic electrolyte system. Chae et al. [121] synthesized a high-voltage electrode material, $K_{0.86}Ni[Fe(CN)_6]_{0.954}(H_2O)_{0.766}$, through electrochemically removing K^+ from the lattice, and its electrochemical performance was tested with 0.5 M $Mg(ClO_4)_2$ in acetonitrile. It delivered a discharge capacity of 48.3 mAh g^{-1} and the average discharge voltage was 2.99 V (vs. Mg^{2+}/Mg) at 0.2 C.

Mg^{2+} has two charges which can provide two electrons for the reaction, but this also increases the probability of side reactions and results in the slow kinetics of magnesium ions and the phase transformation of the cathode material, further contributing to low capacity, low voltage, and poor rate performance. However, the slow insertion kinetics would be greatly improved through anion groups and Mg^{2+} co-intercalation [122]. Moreover, it was reported that the water in electrolyte solution could shield the charge of Mg^{2+} ion and improve the poor kinetics [123, 124].

3.2.2. PB/PBAs cathodes for calcium-ion batteries

Calcium is the fifth most abundant element in the earth's crust, which is richer than both sodium and magnesium, and 2500 times more abundant than lithium. In recent years, the researchers have gradually shifted their attention to the study of calcium-ion battery. Calcium-ion battery has several advantages: (1) rich calcium reserves and low cost; (2) the standard electrode potential of calcium metal (−2.87 V, vs. SHE) is closer to that of lithium (−3.04 V, vs. SHE); (3) compared with other multivalent ions, Ca^{2+} has advantages in the kinetics of cathode reactions due to its large ion radius which would lead to low charge density; and (4) the deposition potential of calcium is 0.17 V higher than that of lithium and 0.5 V lower than that of magnesium, which may have higher operating voltage and energy density compared with magnesium [130,131].

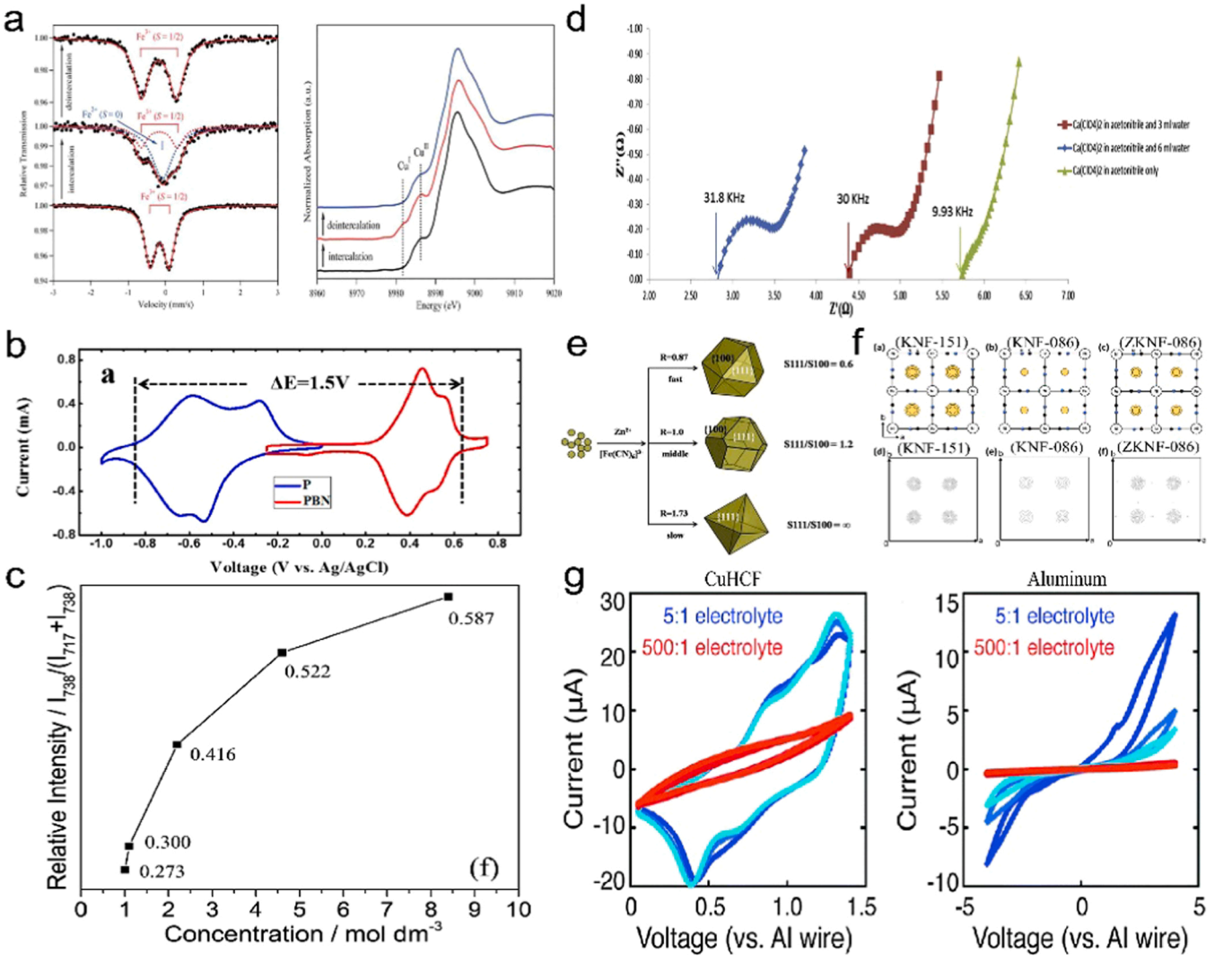

Fig. 7. (a) ^{57}Fe Mössbauer spectra and ex-situ Cu K-edge X-ray absorption spectra. Reprinted with permission. Copyright 2013, The Royal Society of Chemistry [118]. (b) Cyclic voltammetry (CV) curves of PBN and polyimide during the intercalation of Mg^{2+}. Reprinted with permission. Copyright 2017, American Chemical Society [119]. (c) The relation between relative intensity of Raman spectra peak and the $Ca(NO_3)_2$ concentration. Reprinted with permission [125]. Copyright 2018, Elsevier. (d) Nyquist plots for $K_2BaFe(CN)_6$. Reprinted with permission [126]. Copyright 2014, Elsevier. (e) A schematic illustration of the nucleation and growth process of ZnHCF particles. Reprinted with permission [127]. Copyright 2015, Nature. (f) The electron densities at the interstitial (8c) site for (a) $K_{1.51}Ni[Fe(CN)_6]_{0.954}(H2O)_{0.766}$ (KNF-151), $K_{0.86}Ni[Fe(CN)_6]_{0.954}(H2O)_{0.766}$ (KNF-086), and $Zn_{0.32}K_{0.86}Ni[Fe(CN)_6]_{0.954}(H2O)_{0.766}$ (ZKNF-086). Reprinted with permission [128]. Copyright 2016, Elsevier. (g) CV curves in 5: 1 molar ratio diglyme: aluminum electrolyte and 500: 1 molar ratio diglyme: aluminum electrolyte of a CuHCF electrode and an aluminum electrode. Reprinted with permission [129]. Copyright 2015, The Royal Society of Chemistry.

Wang et al. [132] demonstrated that the open framework of NiHCF could insert Ca^{2+} reversibly. The calcium-ion full cell was composed of the NiHCF cathode, the activated carbon counter electrode with 1 M calcium nitrate solution. 53% of the initial capacity was remained after 2000 cycles at 5 C at a voltage range of 0.22–0.92 V. Lee and Jeong et al. [125] investigated the influence of the concentration change of electrolyte ($Ca(NO_3)_2$) in the aqueous electrolyte on the performance of calcium-ion battery with $CuFe(CN)_6$ as the cathode material. The relation between relative intensity of Raman spectra peak and the $Ca(NO_3)_2$ concentration (Fig. 7c) shows that increasing the concentration of $Ca(NO_3)_2$ can enhance the coordination number of Ca^{2+} and NO_3^-, thus reducing the hydration number of Ca^{2+} through structural change of the electrolyte. Therefore, Ca^{2+} with small hydration number and small radius can be repeated intercalation/deintercalation into CuHCF, which results in the increase of discharge/charge capacities. On the other hand, the high concentration of electrolyte can reduce the activation energy of calcium ion inserted into the CuHCF electrode, thus improving the electrochemical performance. When the electrolyte is 8.4 M, after 5000 cycles at 10 C, this battery can achieve ~88.6% of the capacity with 98.1% of the coulombic efficiency, which is better than in 1 M electrolyte solution.

The dissolution of the cathode material into aqueous electrolyte seemed to be an obstacle in the development of calcium-ion batteries because solvent molecules with higher donor numbers exhibited a stronger cationic solvation in the electrolyte, and the donor number (DN) of water was higher than that of the propylene carbonate (PC) in the study of the quantitative determination of the Lewis alkalinity of the DN [133,134]. In addition, it was reported that the enthalpy of hydration of water molecules was lower than the enthalpy of solvation of PC molecules [135]. Therefore, for the limitation of aqueous electrolyte, Lee et al. [136] adopted a mixture of water and propylene carbonate (PC) containing $Ca(CF_3SO_3)_2$ to improve the electrochemical performance of CuHCF cathode in calcium-ion battery. The results showed that when the molar ratio of calcium ions to water in the electrolyte was 1:6, the cathode showed a higher capacity (~65 mAh g^{-1}). In addition, the coulombic efficiency of the electrode above 800 cycles was about

100%, and the maximum capacity retention was about 94% after 800 cycles, with a charge capacity retention of 52% at 10 C.

Tojo et al. [137] reported a $K_xNiFe(CN)_6$ cathode material, which was tested in 0.5 M calcium bis-trifluoromethylsulfonylimide ($Ca(TFSI)_2$) dissolved in acetonitrile organic electrolyte. Calcium-ion could be reversibly inserted into KNiFe-PBA and the reversible capacity was 40 mAh g^{-1} after 12 cycles. Subsequently, the electrochemical behavior of Ca^{2+} in the intercalation process was explored by means of XRD and XPS characterization techniques. The results showed that after the first discharge, the intensity and position of Fe^{2+} and Ni^{2+} were restored to their initial states, indicating the charge compensation of the reversible Fe^{3+}/Fe^{2+} and Ni. Therefore, Ca^{2+} reversibly entering the frame interstitial site of $K_xNiFe(CN)_6$ could be ensured and the structural stability during intercalation could be maintained as well.

Padigi et al. [126] synthesized a ($K_2BaFe(CN)_6$) by chemical precipitation and used it as the cathode material of calcium-ion batteries. Through introducing a small amount of water into the organic electrolyte (1 M $Ca(ClO_4)_2$ in acetonitrile), the hydration sphere formed around Ca^{2+} could shield the influence of the strong coulomb interaction between Ca^{2+} and CN^- in ($K_2BaFe(CN)_6$), and alleviated the problems of poor intercalation and/or diffusion of the cations as well as the large degree of polarization (Fig. 7d). The charge-discharge mechanism of this $K_2BaFe(CN)_6$ was found to be as follows:

$$K_2BaFe^{II}(CN)_6 \rightarrow KBaFe^{III}(CN)_6 + K^+ + e^- \text{ (first charge cycle)} \quad (1)$$

$$KBaFe^{III}(CN)_6 + 0.5\ Ca^{2+} + e^- \text{ (charging)} \rightarrow Ca_{0.5}KBaFe^{II}(CN)_6 \text{ (discharging)} \quad (2)$$

where Eq. (1) represents the charging reaction of the first cycle; Eq. (2) represents the subsequent charge/discharge cycle reaction. At the end of 30 cycles, the reversible ratio was 55.8 mAh g^{-1}, which was about 80% of the estimated theoretical capacity of 70 mAh g^{-1} with the coulomb efficiency of 93.8%.

Due to the strong electrostatic interaction between calcium ion and host material, the diffusion efficiency of Ca-ion is low. In addition, the research progress in electrode and electrolyte of calcium-ion battery is relatively slow. Constructing high-performance calcium-ion batteries is still at its early stage.

3.2.3. PB/PBAs cathodes in zinc-ion batteries

The successful intercalation of Zn^{2+} in PB/PBAs makes them the potential cathode material for zinc-ion batteries. As a new type of multivalent ion rechargeable batteries, zinc-ion batteries have the following advantages: (1) abundant zinc resource in the earth crust and low price; (2) zinc has low redox potential (−0.76 V vs. SHE) and high hydrogen evolution overpotential, which makes it electrochemically stable in aqueous solution; (3) high theoretical capacity of zinc anode (819 mAh g^{-1}); (4) Zn-ion radius is 0.74 Å, which is less than the radius of sodium-ion (1.02 Å) and close to that of lithium-ion (0.69 Å), which is conducive to the kinetic behavior; and (5) low toxicity and environmentally-friendly [143,144].

Trocoli et al. [139] developed an aqueous zinc-ion battery with $K_{0.71}Cu[Fe(CN)_6]_{0.72}\cdot 3.7H_2O$ (CuHCF) as the cathode, Zn foil as the anode and 20 mM zinc sulfate ($ZnSO_4$) as the electrolyte. It delivered an average discharge potential of 1.73 V with a capacity retention of 96.3% after 100 cycles at 1 C.

ZnHCF is considered to be a material capable of effectively intercalating zinc ion. Compared with most cubic structures of MHCF, ZnHCF has a dimorphic (cubic or rhombohedral) structure, in which ZnN_4 tetrahedron is connected with FeC_6 octahedron through CN ligand to form a porous three-dimensional structure that can hold metal ions. Zhang et al. [140] obtained $Zn_3[Fe(CN)_6]_2$ (ZnHCF) by high temperature coprecipitate and assembled a zinc-ion battery ($Zn/ZnSO_4/ZnHCF$). The reactions of charge and discharge were expressed as:

$$\text{Cathode: } \lambda Zn^{2+} + 2\lambda e^- + Zn_3[Fe(CN)_6]_2 \leftrightarrow Zn_{3+\lambda}[Fe(CN)_6]_2 \quad (3)$$

$$\text{Anode: } \lambda Zn \leftrightarrow \lambda Zn^{2+} + 2\lambda e^- \quad (4)$$

Where λ represents the number of Zn^{2+} that can be reversibly inserted into ZnHCF. The theoretical capacity was 65.4 mAh g^{-1} at 1 C and the average working voltage was 1.7 V. The influence of the morphology and interface on the electrochemical performance of ZnHCF was also studied by adjusting the drop acceleration of the mixing reaction, where ZnHCF was synthesized into cubooctahedral, truncated octahedron, and octahedron morphologies, respectively. The uniform nucleation and growth of crystals were obtained with 0.01 M $ZnSO_4$ and 0.01 M $K_3Fe(CN)_6$ (Fig. 7e)[127]. The results showed that the cycling stability and rate performance of the cubooctahedral (C-RZnHCF) were better than those of the other two morphologies. On the one hand, the growth orientation of the cubic octahedron was closer to the surface of the $< 100 >$ arranged by the zinc ion diffusion channel, which accelerated the kinetic process and increased the rate performance. On the other hand, the cubooctahedral had less $< 111 >$ orientation, which reduced the interaction with the electrolyte. Subsequently, the efficient reversible interlayer of Zn^{2+} in C-RZnHCF was proved by XRD. In the full battery assembled with zinc anode, the obtained average working voltage was 1.73 V with a discharge capacity of 66.5 mAh g^{-1}.

In general, the working voltage of the zinc-ion battery is limited by the voltage window of aqueous electrolyte. In addition, the corrosion and deactivation of the zinc anode surface by the acidity and alkalinity of the aqueous solution also need to be further solved. For this purpose, the researchers have developed zinc-ion batteries of organic liquid electrolyte [132,139]. For example, $K_{0.86}Ni[Fe(CN)_6]_{0.954}(H_2O)_{0.766}$ as the cathode material in organic electrolyte was reported by Chae et al. [128]. The electrochemical performances of this material were tested with 0.5 M $Zn(ClO_4)_2$ in acetonitrile (AN) as the organic electrolyte and zinc as the anode. As shown in Fig. 7f, decreasing K^+ content in the cavity can reduce the attraction of Zn^{2+} with negatively charged CN^- in the intercalation process, and reduced the electron density, thus improving the electrochemical performance of the material. The results showed that the cycling efficiency of the organic electrolyte system (>99.9%) was higher than that of the aqueous system (about 80%). At 0.2 C, the reversible discharge capacity of the battery was 55.6 mAh g^{-1} at the discharge voltage of 1.19 V (vs. Zn^{2+}/Zn).

Liu et al. [138] used the biodegradable and biocompatible ionic liquid as the organic electrolyte ($Zn(OAc)_2$/([Ch]OAc+30 wt% water)), $K_{0.05}Fe(III)[Fe(III)(CN)_6]\cdot 2.6H_2O$ as the cathode material and zinc as the anode material to construct a zinc-ion battery. The reversible discharge capacity of this battery at 10 mA g^{-1} (~0.1 C) was 120 mAh g^{-1} with a coulombic efficiency of 99%.

However, PB/PBAs show relatively low capacities and fast decay when applied in Zn^{2+} batteries. Deng et al. [145] found that the insertion of high charge density Zn^{2+} could induce and intensified the Jahn-Teller effect of manganese in the storage of Zn^{2+} in the $K_2MnFe(CN)_6$, and also participated in the formation of new phases, leading to the transformation of structure and phase. The original monoclinic material ($K_2MnFe(CN)_6$) was completely transformed into another rhomboidal material ($K_2Zn_3[Fe(CN)_6]_2$). Interestingly, the transformed structure was more suitable for storing Zn^{2+}. It could achieve 100 mAh g^{-1} after 400 cycles at 0.2 A g^{-1} in 30 m KFSI + 1 m $Zn(CF_3SO_3)_2$ electrolyte.

Although PBAs have low specific capacities in zinc-ion batteries, they have high discharge voltages. In the future, PBAs anode materials with high output capacity and excellent cycling stability should be developed for zinc-ion batteries, which would enable them to be a new choice for large-scale grid energy storage systems [146–148].

3.2.4. PB/PBAs cathodes for aluminum-ion batteries

In principle, aluminum-ion battery can be used as a new potential rechargeable battery because aluminum has several advantages: (1) three-electron redox reaction can occur, resulting in a large volume

capacity (8.04 Ah cm^{-3}); (2) relatively high mass capacity (2.98 Ah g^{-1}); (3) abundant resources and readily availability (7.45%, 1200 times higher than Li); and (4) environmental friendliness [141].

Although aluminum-ion battery has the above advantages, the development of aluminum-ion battery is still facing big challenges, the current research is only at the premature stage. Some seemingly advantages of aluminum-ion battery are also the sources of disadvantages: (1) the small diameter of aluminum ion and the high valence state, which can easily produce a strong electrostatic effect with the cathode matrix structure, resulting in low transmission and structural instability, further leading to rapid electrochemical degradation of capacity; (2) the application of aluminum in the aqueous electrolyte is limited because its electrochemical plating/stripping voltage is too far from the stable potential window of water; and (3) most of the aqueous electrolytes studied are highly acidic, which can accelerate the dissolution of the cathode material and the corrosion of the equipment and greatly reduce the cycling stability and safety in use [149].

Despite the successful insertion of the monovalent and divalent cations into the PB/PBAs frameworks, the insertion reaction of trivalent cation has a strong charge effect on the materials [150]. Thus, the cathode reactions are barriered by the slow kinetics of solid-state diffusion and intrinsically high charge density of multivalent Al^{3+} [151]. Liu et al. [150] used copper hexacyanoferrate (CuHCF) as the cathode material for an aqueous aluminum-ion battery. The results prove that though the strong bonding between Al^{3+} ion and CN ligand could hinder the Al^{3+} ion transfer in the CuHCF framework, the insertion of Al^{3+} ion in CuHCF was still realized through a shield charge concentration induced by residual zeolitic water. Reed et al. [129] selected CuHCF as the cathode material of aluminum-ion battery and studied the method of reversible aluminum intercalation/deintercalation into CuHCF in the organic electrolytic liquid system of aluminum trifluoromethanesulfonate (aluminum triflate) dissolved in diethylene glycol dimethyl ether (diglyme). According to the charge-discharge profile of CuHCF, it can be seen that the inclined discharge potential and large lagging voltage are the kinetic obstruction of Al^{3+} during intercalation. By comparing with the electrolyte of diglyme: aluminum triflate with different molar ratios (5:1 vs. 500:1) (Fig. 7g), it could be found that CuHCF exhibited the electrochemical activity only in high concentration electrolytes. In addition, for aluminum anode in a high concentration of aluminum triflate, although it can lead to the rapid deactivation of aluminum and the difficult transfer of Al^{3+}, it can enhance the electrode activity. The anode delivered a poor reversible capacity (14 mAh g^{-1}). This was because that it was not the naked Al^{3+} that intercalated, but a diglyme-chelated aluminum ion ($Al(Di)_2^{3+}$)) which was a stable complex formed by aluminum triflate and diglyme. In addition, XRD analysis proved that the insertion of ($Al(Di)_2^{3+}$) in the cycling process could lead to the pulverization of CuHCF crystal and the degradation of the cycling performance.

An aluminum-ion battery was assembled by Gao et al. [141] with potassium nickel hexacyanoferrate (KNHCF) as the cathode material, aluminum foil as the anode material, and $Al(OTf)_3$ aqueous solution as the electrolyte. Through various characterization techniques, it was found that during the process of Al^{3+} reversible intercalation/deintercalation, a single-phase redox reaction of Fe and Ni was accompanied. In addition, the dissolution of Ni in KNHCF could improve the average valence state of Fe in the structure and exposed more iron ions in the electrolyte, increasing the interface reaction, and producing the compensation effect of mixed redox center on KNHCF and making contribution to the capacity. Cycling within the voltage range of 0.2–1.1 V at a current density of 20 mA g^{-1} after 500 cycles, the initial discharge capacity was 46.5 mAh g^{-1} and the capacity remained about half.

Ru et al. [142] synthesized potassium cobalt hexacyanoferrate ($K_2CoFe(CN)_6$) with a nanoscale cubic assembly structure by one-step hydrothermal method and low temperature calcining method, and used as the cathode material of the aluminum-ion battery. The reactions in the battery were described as follows:

$$\text{Charging: } Al_{2/3}Co^{II}Fe^{II}(CN)_6 \rightarrow Co^{III}Fe^{III}(CN)_6 + 2/3Al^{3+} + 2e^- \quad (5)$$

$$\text{Discharging: } Co^{III}Fe^{III}(CN)_6 + 2/3Al^{3+} + 2e^- \rightarrow Al_{2/3}Co^{II}Fe^{II}(CN)_6 \quad (6)$$

With $Al(NO_3)_3$ as the aqueous electrolyte, the reversible discharge capacity of 50 mAh g^{-1} at 0.1 A $g^{-1}$was obtained, and the capacity retention was 76% after 1600 cycles.

Currently, there are only very few researches on PB/PBAs for aluminum-ion batteries, so it is still necessary to explore the feasibility of this new battery system.

4. Industrial manufacture

In recent years, PBAs have attracted extensive attention from researchers, and the development of materials with excellent performance has continuously promoted the progress of commercialization. Among different kinds of PBAs, Fe-based PBAs and Mn-based PBAs have been regarded as the very promising materials due to their rich resources and low prices. Moreover, the facile room temperature precipitation synthesis methods of PBAs make themselves very competitive in large scale production rather than by energy-consuming high-temperature calcination or complex hydrothermal method. Notably, the scale up production of PABs has been proved to have limited impact on electrochemical performance or overall quality [152]. In addition, most of the conventional facilities manufactured in LIBs can be used for PBAs slurry mixing and processing without constructing the entirely new production equipment and production lines. Although PBAs have shown potential applications in both non-aqueous and aqueous rechargeable batteries based on other alkali metal ions (K^+) or polyvalent cations (Zn^{2+}, Mg^{2+}, Al^{3+}, etc.), the unsatisfactory electrochemical performance tested and the relatively slow kinetic behavior observed limit the future development of PBAs materials for these batteries in the short term [153,154]. As a result, SIBs have become the primary low-cost battery systems developed by using PBAs. There are several start-up SIBs companies focusing on the commercialization of PBAs: Novasis Energies, Inc. (USA) and Liaoning Starry Sky Sodium-ion Battery Co., Ltd. (China), which applied $Na_xMnFe(CN)_6$ (Mn-PBA) and $Na_xFeFe(CN)_6$ (Fe-PBA) as the cathode materials, respectively [152]. For example, Liaoning Starry Sky Sodium-ion Battery Co., Ltd. (China) further improved the specific capacity to more than 100mAhg^{-1} by optimizing the synthesis strategy. The largest Li-ion EV battery enterprise, Contemporary Amperex Technology (CATL) unveiled the first generation of PBAs as the cathode material in July 2021, achieving a full battery energy density of 160 Wh kg^{-1} with high rate and low temperature performance.

5. Potential toxicity of PB/PBAs for metal-ion batteries

The broad application prospect of PB/PBAs in rechargeable batteries has been demonstrated in the previous sections. Although they are considered to be the thermally stable molecules, they are composed of toxic cyanide. Whether the cyanide would be released during production and usage and cause poisoning effect needs to be considered before industrialization [155]. In order to further understand whether the materials are suitable for industrial production and long-term use, their potential toxicity should be carefully evaluated. The release behavior of cyanide is mainly affected by pH, temperature, exposure time, and synthesis method. Yang et al. [156] studied the releasing behavior of PB in hydrochloric acid solution and proved that under certain pH conditions, PB could decompose free CN^-, through two steps:

$$Fe_4^{III}[Fe^{II}(CN)_6]_3 \leftrightarrow 4Fe^{3+} + 3[Fe^{II}(CN)_6]^{4-} \quad (7)$$

$$3[Fe^{II}(CN)_6]^{4-} \leftrightarrow 3Fe^{2+} + 6CN^- \quad (8)$$

The releasing capacity of cyanide was relatively stable in the case of a neutral solution. When pH was less than 7 or higher than 7, the release amount of cyanide gradually increased with enhancing acidity and alkalinity. When the exposure time was 24 h, the maximum cyanide released was about 135 μg g^{-1}. In the preparation of PB/PBAs, the single-source method was required at a lower pH and the protection measures in the production process needed to be in place. However, the yield of the method is generally low, whether it can be used in industrialization remains to be verified. Aparicio et al. [157] studied the thermal decomposition temperature of PB and found that it began to release $(CN)_2$ in large quantities at about 300 °C, and the decomposition formula were as follows:

$$Fe_4[Fe(CN)_6]_3.4H_2O \leftrightarrow 0.26Fe_4[Fe(CN)_6]_3 + 0.74(7/5Fe_3^{II}[Fe^{III}(CN)_6]_2 + 3/5(CN)_2 + 4H_2O) \quad (9)$$

Therefore, PB is generally stable except at extreme temperatures.

Inoue et al. [158] studied the Mössbauer properties of PB thermal decomposition products in vacuum. It was assumed that the change of Mössbauer parameter above 250 °C was corresponding to the inversion or the existence of mixed valence state of the cyanide ligand. It turned out that PB had not been completely decomposed at such a low temperature. In addition, Peng et al. [27] found that the crystal structure of Mn/Fe-PBAs could be maintained at 260 °C demonstrated by high-resolution synchrotron in situ heated X-ray powder diffraction. By-production of cyanide can be avoided by using a modified coprecipitation method rather than ferrocyanide or ferricyanide in the acid.

A lot of research still needs to be done to study the safety of PB/PBAs in rechargeable metal-ion batteries whether in production mode, battery use, or waste battery treatment, which is of guiding significance for the industrialization of PB/PBAs cathode materials.

6. Recycling of PBAs-based batteries

The establishment of battery production must run in chains with appropriate recycling technologies [159]. A closed loop of battery materials based on scalable production and recycling technologies is a core component of sustainable battery development. To achieve this goal, mechanical, thermal and chemical processes should be used and combined in different ways. For a battery, the recycling process is as follows: after running out of service life, the battery is mechanically disassembled and the components (casing material, positive electrode, negative electrode, etc.) are separated [160,161]. Then, a purification process will proceed with pyrometallurgical or hydrometallurgical processes. For PBAs-based batteries, the main valuable metal elements in the cathode materials are Fe, Mn, Co, etc., which can be separated by hydrometallurgical process. Here, we introduce two routes for the recycling of PBAs:

6.1. Recycling of PBAs

In the process, NaOH can be used to separate the metal precipitates directly. Taking PB as an example, the equation is shown as follows [162]:

$$12OH^- + Fe[Fe(CN)_6]_3 \rightarrow 3Fe(CN)_6^{4-} + 4Fe(OH)_3 \quad (10)$$

$Fe(CN)_6^{4-}$ can infused into the mother liquor for the next round of production, and $Fe(OH)_3$ can also be used as an iron source for production after acidification.

6.2. Recycling of other active materials

Firstly, the electrode material is dissolved in H_2SO_4 for etching, and metal elements such as Fe, Mn and Co are sieved through NaOH. Finally, other metal elements are precipitated by precipitation agent and resynthesized to produce a new active material after the separation. In the process of hydrometallurgy of PBAs-based materials, it should be noted that a large amount of wastewater containing cyanogen will be produced in the cycling process. In industry, such a wastewater can usually be treated by alkaline chlorination and hydrogen peroxide oxidation [163]. Therefore, security is also critical throughout the recycling process.

Besides the recycling of the materials inside the batteries out of use, the discarded materials can be also turned into usable electrode raw material precursors. For example, Peng et al. [164] demonstrated a simple method for transferring rusty iron products into Prussian blue cathode material for SIBs. This work presents an effective strategy for recycling waste chemicals into battery electrodes and provides a new insight for the production and recycling of PBAs based materials.

7. Conclusion and outlook

In summary, this review focuses on the potential industrial prospects of PB/PBAs cathode materials for low-cost rechargeable metal-ion batteries mainly with discussion on the synthesis methods, material structures, electrochemical performances, functional mechanisms and recycling. The traditional chemical co-precipitation method is the most commonly used method to synthesize PB/PBAs materials. However, due to its excessive crystallization rate, there are a lot of defects and crystal water in PB/PBAs lattice, which affect the electrochemical process of the electrode. The addition of a chelating agent and adjusting drying temperature can effectively improve crystallinity. The single source method can increase crystallinity, but it produces more toxic substances during the synthesis process, limiting its commercial development. By contrast, the optimized co-precipitation method will be the preferred method for synthesizing PB/PBAs.

It's worth noting that the functions of defects and crystal water in monovalent metal-ion batteries and multivalent metal-ion batteries are different. For example, their existence can hinder the diffusion of the metal-ion in monovalent metal-ion batteries, while in the multivalent metal-ion battery, the strong electrostatic interaction between positive and negative ions can be alleviated. Thus, the requirements of crystal water content are varied in different battery systems. Studying the crystallization mechanism and controlling the crystallization rate is critical for the development of PB/PBAs to regulate the content of internal crystal water in the future.

Modification strategies can be applied to improve electrochemical performance of the PB/PBAs. For instance, cycling stability can be ameliorated through the coating by improving the conductivities of PB/PBAs (their intrinsic low conductivities can largely affect the rate performance). On the other hand, morphology and size control can shorten the ion diffusion path would boost the kinetic process. Additionally, element doping would be very efficient to tune the band gaps of PB/PBAs, which in turn improve the electrical conductivities. Similarly, the development of the electrolyte is also crucial. The appropriate electrolyte can not only improve the life-span of the PB/PBAs-based batteries, but also ensure the safety in use. Compared with other high-price electrode materials for lithium-ion batteries, the simple and inexpensive material preparation of PB/PBAs is also a potential choice to solve the issue of battery cost. In particular, PB/PBAs can be used in resource-rich and inexpensive battery systems such as sodium-ion and potassium-ion batteries, which will provide a new way for future energy storage. Furthermore, the development of PB/PBAs aqueous batteries can further improve the safety of batteries and enable them to be competitive candidates for grid-scale energy storage. In the future, it is important to use low-cost and environmentally friendly elements such as Mn, Fe, etc. and develop a safe and efficient synthesis method for large-scale production, which can promote the industrialization of PB/PBAs.

The development of PB/PBAs materials has provided a broad prospect for the field of battery energy storage. We hope that this review can provide an insightful research overview of PB/PBAs materials for research and development of metal-ion batteries.

Declaration of Competing Interest

The authors declare that they have no known competing financial interests or personal relationships that could have appeared to influence the work reported in this paper.

Acknowledgments

This work is financially supported by the National Natural Science Foundation of China (Nos. 21601122, 21671128, 51803116), the Belt and Road Initiatives International Cooperation Project (No. 20640770300).

References

[1] K.S. Pei, C.Y. Wang, J.J. Zhang, Electrochemical Energy: Advanced Materials and Technologies, CRC Press, 2017.
[2] D. Kundu, E. Talaie, V. Duffort, L.F. Nazar, The emerging chemistry of sodium ion batteries for electrochemical energy storage, Angew. Chem. Int. Ed. Engl. 54 (2015) 3431–3448, https://doi.org/10.1002/anie.201410376.
[3] F. Dou, L. Shi, G. Chen, D. Zhang, Silicon/carbon composite anode materials for lithium-ion batteries, Electrochem. EnergyRev. 2 (2019) 149–198, https://doi.org/10.1007/s41918-018-00028-w.
[4] P.E. Lokhande, U.S. Chavan, A. Pandey, Materials and fabrication methods for electrochemical supercapacitors: overview, Electrochem. Energy Rev. 3 (2019) 155–186, https://doi.org/10.1007/s41918-019-00057-z.
[5] H. Wu, C. Feng, L. Zhang, J. Zhang, D.P. Wilkinson, Non-noble metal electrocatalysts for the hydrogen evolution reaction in water electrolysis, Electrochem. Energy Rev. (2021), https://doi.org/10.1007/s41918-020-00086-z.
[6] M. Armand, J.M. Tarascon, Building better batteries, Nature 451 (2008) 652–657, https://doi.org/10.1038/451652a.
[7] J. Li, X. Cao, A. Pan, Y. Zhao, H. Yang, G. Cao, S. Liang, Nanoflake-assembled three-dimensional $Na_3V_2(PO_4)_3$/C cathode for high performance sodium ion batteries, Chem. Eng. J. 335 (2018) 301–308, https://doi.org/10.1016/j.cej.2017.10.164.
[8] X. Wu, W. Deng, J. Qian, Y. Cao, X. Ai, H. Yang, Single-crystal $FeFe(CN)_6$ nanoparticles: a high capacity and high rate cathode for Na-ion batteries, J. Mater. Chem. A 1 (2013), https://doi.org/10.1039/c3ta12036h.
[9] C. Zhang, Y. Xu, M. Zhou, L. Liang, H. Dong, M. Wu, Y. Yang, Y. Lei, Potassium prussian blue nanoparticles: a low-cost cathode material for potassium-ion batteries, Adv. Funct. Mater. 27 (2017), 1604307, https://doi.org/10.1002/adfm.201604307.
[10] L. Deng, T. Wang, Y. Hong, M. Feng, R. Wang, J. Zhang, Q. Zhang, J. Wang, L. Zeng, Y. Zhu, L. Guo, A nonflammable electrolyte enabled high performance $K_{0.5}MnO_2$ cathode for low-cost potassium-ion batteries, ACS Energy Lett. 5 (2020) 1916–1922, https://doi.org/10.1021/acsenergylett.0c00912.
[11] Y. Lu, L. Wang, J. Cheng, J.B. Goodenough, Prussian blue: a new framework of electrode materials for sodium batteries, Chem. Commun. 48 (2012) 6544–6546, https://doi.org/10.1039/c2cc31777j.
[12] Y. Li, J. Hu, K. Yang, B. Cao, Z. Li, L. Yang, F. Pan, Synthetic control of prussian blue derived nano-materials for energy storage and conversion application, Mater. Today Energy 14 (2019), https://doi.org/10.1016/j.mtener.2019.07.003.
[13] S. Zhao, Z. Guo, K. Yan, X. Guo, S. Wan, F. He, B. Sun, G. Wang, The rise of prussian blue analogs: challenges and opportunities for high-performance cathode materials in potassium-ion batteries, Small Struct. 2 (2020), 2000054, https://doi.org/10.1002/sstr.202000054.
[14] R.Y. Wang, B. Shyam, K.H. Stone, J.N. Weker, M. Pasta, H.-W. Lee, M.F. Toney, Y. Cui, Reversible multivalent (monovalent, divalent, trivalent) ion insertion in open framework materials, Adv. Energy Mater. 5 (2015), 1401869, https://doi.org/10.1002/aenm.201401869.
[15] C.D. Wessells, S.V. Peddada, M.T. McDowell, R.A. Huggins, Y. Cui, The effect of insertion species on nanostructured open framework hexacyanoferrate battery electrodes, J. Electrochem. Soc. 159 (2011) A98–A103, https://doi.org/10.1149/2.060202jes.
[16] F. Ma, Q. Li, T. Wang, H. Zhang, G. Wu, Energy storage materials derived from Prussian blue analogues, Sci. Bull. 62 (2017) 358–368, https://doi.org/10.1016/j.scib.2017.01.030.
[17] G. Du, H. Pang, Recent advancements in prussian blue analogues: preparation and application in batteries, Energy Storage Mater. 36 (2021) 387–408, https://doi.org/10.1016/j.ensm.2021.01.006.
[18] J. Qian, C. Wu, Y. Cao, Z. Ma, Y. Huang, X. Ai, H. Yang, Prussian blue cathode materials for sodium-ion batteries and other ion batteries, Adv. Energy Mater. 8 (2018), https://doi.org/10.1002/aenm.201702619.
[19] J. Chen, L. Wei, A. Mahmood, Z. Pei, Z. Zhou, X. Chen, Y. Chen, Prussian blue, its analogues and their derived materials for electrochemical energy storage and conversion, Energy Storage Mater. 25 (2020) 585–612, https://doi.org/10.1016/j.ensm.2019.09.024.
[20] F. Herren, P. Fischer, A. Ludi, W. Haelg, Neutron diffraction study of prussian blue, $Fe_4[Fe(CN)_6]_3.xH_2O$. Location of water molecules and long-range magnetic order, Inorg. Chem. 19 (1980) 956–959, https://doi.org/10.1021/ic50206a032.
[21] H.B. Weiser, W.O. Milligan, J.B. Bates, X-ray diffraction studies on heavy-metal iron-cyanides, J. Phys. Chem. B 46 (1942) 99–111, https://doi.org/10.1021/j150415a013.
[22] J.F. Keggin, F.D. Miles, Structures and formulæ of the prussian blues and related compounds, Nature 137 (1936) 577–578, https://doi.org/10.1038/137577a0.
[23] H.J. Buser, D. Schwarzenbach, W. Petter, A. Ludi, The crystal structure of prussian blue: $Fe_4[Fe(CN)_6]_3$ dot xH_2O, Inorg. Chem. 16 (1977) 2704–2709.
[24] S.-H. Lee, Y.-D. Huh, Preferential evolution of prussian blue's morphology from cube to hexapod, Bull. Korean Chem. Soc. 33 (2012) 1078–1080, https://doi.org/10.5012/bkcs.2012.33.3.1078.
[25] T. Shibata, Y. Moritomo, Ultrafast cation intercalation in nanoporous nickel hexacyanoferrate, Chem. Commun. 50 (2014) 12941–12943, https://doi.org/10.1039/c4cc04564e.
[26] J. Nordstrand, E. Toledo-Carrillo, S. Vafakhah, L. Guo, H.Y. Yang, L. Kloo, J. Dutta, Ladder mechanisms of ion transport in prussian blue analogues, ACS Appl. Mater. Interfaces 14 (2021) 1102–1113, https://doi.org/10.1021/acsami.1c20910.
[27] J. Peng, W. Zhang, Z. Hu, L. Zhao, C. Wu, G. Peleckis, Q. Gu, J.Z. Wang, H.K. Liu, S.X. Dou, S. Chou, Ice-assisted synthesis of highly crystallized prussian blue analogues for all-climate and long-calendar-life sodium ion batteries, Nano Lett. 22 (2022) 1302–1310, https://doi.org/10.1021/acs.nanolett.1c04492.
[28] A. Kumar, S.M. Yusuf, L. Keller, Structural and magnetic properties of $Fe[Fe(CN)_6]\bullet 4H_2O$, Phys. Rev. B 71 (2005), https://doi.org/10.1103/PhysRevB.71.054414.
[29] Y. You, X.-L. Wu, Y.-X. Yin, Y.-G. Guo, High-quality prussian blue crystals as superior cathode materials for room-temperature sodium-ion batteries, Energy Environ. Sci. 7 (2014) 1643–1647, https://doi.org/10.1039/c3ee44004d.
[30] X. Wu, M. Shao, C. Wu, J. Qian, Y. Cao, X. Ai, H. Yang, Low defect $FeFe(CN)_6$ framework as stable host material for high performance Li-ion batteries, ACS Appl. Mater. Interfaces 8 (2016) 23706–23712, https://doi.org/10.1021/acsami.6b06880.
[31] X. Wu, C. Wu, C. Wei, L. Hu, J. Qian, Y. Cao, X. Ai, J. Wang, H. Yang, Highly crystallized $Na_2CoFe(CN)_6$ with suppressed lattice defects as superior cathode material for sodium-ion batteries, ACS Appl. Mater. Interfaces 8 (2016) 5393–5399, https://doi.org/10.1021/acsami.5b12620.
[32] C.H. Li, Y. Nanba, D. Asakura, M. Okubo, D.R. Talham, Li-ion and Na-ion insertion into size-controlled nickel hexacyanoferrate nanoparticles, RSC Adv. 4 (2014), https://doi.org/10.1039/c4ra03296a.
[33] X. Wu, M. Sun, S. Guo, J. Qian, Y. Liu, Y. Cao, X. Ai, H. Yang, Vacancy-free prussian blue nanocrystals with high capacity and superior cyclability for aqueous sodium-ion batteries, ChemNanoMat 1 (2015) 188–193, https://doi.org/10.1002/cnma.201500021.
[34] H. Minowa, Y. Yui, Y. Ono, M. Hayashi, K. Hayashi, R. Kobayashi, K.I. Takahashi, Characterization of Prussian blue as positive electrode materials for sodium-ion batteries, Solid State Ion. 262 (2014) 216–219, https://doi.org/10.1016/j.ssi.2013.12.024.
[35] S. Kjeldgaard, I. Dugulan, A. Mamakhel, M. Wagemaker, B.B. Iversen, A. Bentien, Strategies for synthesis of Prussian blue analogues, R. Soc. Open Sci. 8 (2021), 201779, https://doi.org/10.1098/rsos.201779.
[36] R. Chen, Y. Huang, M. Xie, Z. Wang, Y. Ye, L. Li, F. Wu, Chemical inhibition method to synthesize highly crystalline prussian blue analogs for sodium-ion battery cathodes, ACS Appl. Mater. Interfaces 8 (2016) 31669–31676, https://doi.org/10.1021/acsami.6b10884.
[37] Y. Liu, Y. Qiao, W. Zhang, Z. Li, X. Ji, L. Miao, L. Yuan, X. Hu, Y. Huang, Sodium storage in Na-rich $Na_xFeFe(CN)_6$ nanocubes, Nano Energy 12 (2015) 386–393, https://doi.org/10.1016/j.nanoen.2015.01.012.
[38] L. Wang, J. Song, R. Qiao, L.A. Wray, M.A. Hossain, Y.D. Chuang, W. Yang, Y. Lu, D. Evans, J.J. Lee, S. Vail, X. Zhao, M. Nishijima, S. Kakimoto, J.B. Goodenough, Rhombohedral prussian white as cathode for rechargeable sodium-ion batteries, J. Am. Chem. Soc. 137 (2015) 2548–2554, https://doi.org/10.1021/ja510347s.
[39] Y. Liu, G. Wei, M. Ma, Y. Qiao, Role of acid in tailoring prussian blue as cathode for high-performance sodium-ion battery, Chemistry 23 (2017) 15991–15996, https://doi.org/10.1002/chem.201703081.
[40] A. Gong, Y. Zhao, M. He, B. Liang, K. Li, High-performance desalination of three-dimensional nitrogen-doped carbon framework reinforced Prussian blue in capacitive deionization, Desalination 505 (2021), https://doi.org/10.1016/j.desal.2021.114997.
[41] D. Zuo, C. Wang, J. Han, J. Wu, H. Qiu, Q. Zhang, Y. Lu, Y. Lin, X. Liu, Oriented formation of a prussian blue nanoflower as a high performance cathode for sodium ion batteries, ACS Sustain. Chem. Eng. 8 (2020) 16229–16240, https://doi.org/10.1021/acssuschemeng.0c05466.
[42] B. He, P. Man, Q. Zhang, C. Wang, Z. Zhou, C. Li, L. Wei, Y. Yao, Conversion synthesis of self-standing potassium zinc hexacyanoferrate arrays as cathodes for high-voltage flexible aqueous rechargeable sodium-ion batteries, Small 15 (2019), e1905115, https://doi.org/10.1002/smll.201905115.
[43] W. Gong, M. Wan, R. Zeng, Z. Rao, S. Su, L. Xue, W. Zhang, Y. Huang, Ultrafine prussian blue as a high-rate and long-life sodium-ion battery cathode, Energy Technol. 7 (2019), https://doi.org/10.1002/ente.201900108.
[44] W. Gong, R. Zeng, S. Su, M. Wan, Z. Rao, L. Xue, W. Zhang, Ball-milling synthesis of ultrafine $Na_yFe_xMn_{1-x}[Fe(CN)_6]$ as high-performance cathode in sodium-ion batteries, J. Nanopart. Res. 21 (2019), https://doi.org/10.1007/s11051-019-4717-9.
[45] A. Zhou, W. Cheng, W. Wang, Q. Zhao, J. Xie, W. Zhang, H. Gao, L. Xue, J. Li, Hexacyanoferrate-type prussian blue analogs: principles and advances toward high-performance sodium and potassium ion batteries, Adv. Energy Mater. 11 (2020), https://doi.org/10.1002/aenm.202000943.

[46] X.-H. Ma, Y.-Y. Wei, J.-F. Zhou, J.-H. Zhou, S.-W. Zhao, W. Jia, J.-M. Dai, Z.-F. Zi, Low-defect $Na_2Co[Fe(CN)_6]$ synthesized by a facile electrostatic spray assisted coprecipitation method as cathode for sodium-ion batteries, Electrochim. Acta 272 (2018) 44–51, https://doi.org/10.1016/j.electacta.2018.03.181.

[47] Y. Fang, L. Xiao, Z. Chen, X. Ai, Y. Cao, H. Yang, Recent advances in sodium-ion battery materials, Electrochem. Energy Rev. 1 (2018) 294–323, https://doi.org/10.1007/s41918-018-0008-x.

[48] M. Pasta, C.D. Wessells, R.A. Huggins, Y. Cui, A high-rate and long cycle life aqueous electrolyte battery for grid-scale energy storage, Nat. Commun. 3 (2012) 1149, https://doi.org/10.1038/ncomms2139.

[49] B. Dunn, H. Kamath, J.M. Tarascon, Electrical energy storage for the grid: a battery of choices, Science 334 (2011) 928–935, https://doi.org/10.1126/science.1212741.

[50] H.-W. Lee, R.Y. Wang, M. Pasta, S. Woo Lee, N. Liu, Y. Cui, Manganese hexacyanomanganate open framework as a high-capacity positive electrode material for sodium-ion batteries, Nat. Commun. 5 (2014), https://doi.org/10.1038/ncomms6280.

[51] W.-J. Li, C. Han, W. Wang, F. Gebert, S.-L. Chou, H.-K. Liu, X. Zhang, S.-X. Dou, Commercial prospects of existing cathode materials for sodium ion storage, Adv. Energy Mater. 7 (2017), https://doi.org/10.1002/aenm.201700274.

[52] J. Qian, M. Zhou, Y. Cao, X. Ai, H. Yang, Nanosized $Na_4Fe(CN)_6$/C composite as a low-cost and high-rate cathode material for sodium-ion batteries, Adv. Energy Mater. 2 (2012) 410–414, https://doi.org/10.1002/aenm.201100655.

[53] L. Wang, Y. Lu, J. Liu, M. Xu, J. Cheng, D. Zhang, J.B. Goodenough, A superior low-cost cathode for a Na-ion battery, Angew. Chem. Int. Ed. Engl. 52 (2013) 1964–1967, https://doi.org/10.1002/anie.201206854.

[54] M. Takachi, T. Matsuda, Y. Moritomo, Cobalt hexacyanoferrate as cathode material for Na^+ secondary battery, Appl. Phys. Express 6 (2013), https://doi.org/10.7567/apex.6.025802.

[55] X. Bie, K. Kubota, T. Hosaka, K. Chihara, S. Komaba, Synthesis and electrochemical properties of Na-rich prussian blue analogues containing Mn, Fe, Co, and Fe for Na-ion batteries, J. Power Sources 378 (2018) 322–330, https://doi.org/10.1016/j.jpowsour.2017.12.052.

[56] H.W. Lee, R.Y. Wang, M. Pasta, S. Woo Lee, N. Liu, Y. Cui, Manganese hexacyanomanganate open framework as a high-capacity positive electrode material for sodium-ion batteries, Nat. Commun. 5 (2014) 5280, https://doi.org/10.1038/ncomms6280.

[57] Y. Yang, E. Liu, X. Yan, C. Ma, W. Wen, X.-Z. Liao, Z.-F. Ma, Influence of structural imperfection on electrochemical behavior of prussian blue cathode materials for sodium ion batteries, J. Electrochem. Soc. 163 (2016) A2117–A2123, https://doi.org/10.1149/2.0031610jes.

[58] W.-J. Li, S.-L. Chou, J.-Z. Wang, Y.-M. Kang, J.-L. Wang, Y. Liu, Q.-F. Gu, H.-K. Liu, S.-X. Dou, Facile method to synthesize Na-enriched $Na_{1+x}FeFe(CN)_6$ frameworks as cathode with superior electrochemical performance for sodium-ion batteries, Chem. Mater. 27 (2015) 1997–2003, https://doi.org/10.1021/cm504091z.

[59] M. Hu, S. Ishihara, K. Ariga, M. Imura, Y. Yamauchi, Kinetically controlled crystallization for synthesis of monodispersed coordination polymer nanocubes and their self-assembly to periodic arrangements, Chemistry 19 (2013) 1882–1885, https://doi.org/10.1002/chem.201203138.

[60] Y. You, X. Yu, Y. Yin, K.-W. Nam, Y.-G. Guo, Sodium iron hexacyanoferrate with high Na content as a Na-rich cathode material for Na-ion batteries, Nano Res. 8 (2014) 117–128, https://doi.org/10.1007/s12274-014-0588-7.

[61] J. Song, L. Wang, Y. Lu, J. Liu, B. Guo, P. Xiao, J.J. Lee, X.Q. Yang, G. Henkelman, J.B. Goodenough, Removal of interstitial H_2O in hexacyanometallates for a superior cathode of a sodium-ion battery, J. Am. Chem. Soc. 137 (2015) 2658–2664, https://doi.org/10.1021/ja512383b.

[62] D. Yang, J. Xu, X.Z. Liao, H. Wang, Y.S. He, Z.F. Ma, Prussian blue without coordinated water as a superior cathode for sodium-ion batteries, Chem. Commun. 51 (2015) 8181–8184, https://doi.org/10.1039/c5cc01180a.

[63] S.J.R. Prabakar, J. Jeong, M. Pyo, Highly crystalline prussian blue/graphene composites for high-rate performance cathodes in Na-ion batteries, RSC Adv. 5 (2015) 37545–37552, https://doi.org/10.1039/c5ra04769b.

[64] Y. You, X.-L. Wu, Y.-X. Yin, Y.-G. Guo, A zero-strain insertion cathode material of nickel ferricyanide for sodium-ion batteries, J. Mater. Chem. A 1 (2013), https://doi.org/10.1039/c3ta13223d.

[65] M. Xie, M. Xu, Y. Huang, R. Chen, X. Zhang, L. Li, F. Wu, $Na_2Ni_xCo_{1-x}Fe(CN)_6$: a class of prussian blue analogs with transition metal elements as cathode materials for sodium ion batteries, Electrochem. Commun. 59 (2015) 91–94, https://doi.org/10.1016/j.elecom.2015.07.014.

[66] Q. Meng, W. Zhang, M. Hu, J.S. Jiang, Mesocrystalline coordination polymer as a promising cathode for sodium-ion batteries, Chem. Commun. 52 (2016) 1957–1960, https://doi.org/10.1039/c5cc08754f.

[67] W. Ren, M. Qin, Z. Zhu, M. Yan, Q. Li, L. Zhang, D. Liu, L. Mai, Activation of sodium storage sites in prussian blue analogues via Surface Etching, Nano Lett. 17 (2017) 4713–4718, https://doi.org/10.1021/acs.nanolett.7b01366.

[68] Y. Huang, M. Xie, Z. Wang, Y. Jiang, Y. Yao, S. Li, Z. Li, L. Li, F. Wu, R. Chen, A chemical precipitation method preparing hollow-core-shell heterostructures based on the prussian blue analogs as cathode for sodium-ion batteries, Small 14 (2018), e1801246, https://doi.org/10.1002/smll.201801246.

[69] H. Hu, W. Liu, M. Zhu, Y. Lin, Y. Liu, J. Zhang, T. Chen, K. Liu, Yolk-shell prussian blue nanoparticles with fast ion diffusion for sodium-ion battery, Mater. Lett. 249 (2019) 206–209, https://doi.org/10.1016/j.matlet.2019.04.102.

[70] F. Feng, S. Chen, X.Z. Liao, Z.F. Ma, Hierarchical hollow prussian blue rods synthesized via self-sacrifice template as cathode for high performance sodium ion battery, Small Methods 3 (2018), https://doi.org/10.1002/smtd.201800259.

[71] Y. Jiang, S. Yu, B. Wang, Y. Li, W. Sun, Y. Lu, M. Yan, B. Song, S. Dou, Prussian blue@C composite as an ultrahigh-rate and long-life sodium-ion battery cathode, Adv. Funct. Mater. 26 (2016) 5315–5321, https://doi.org/10.1002/adfm.201600747.

[72] Y. You, H.R. Yao, S. Xin, Y.X. Yin, T.T. Zuo, C.P. Yang, Y.G. Guo, Y. Cui, L.J. Wan, J.B. Goodenough, Subzero-temperature cathode for a sodium-ion battery, Adv. Mater. 28 (2016) 7243–7248, https://doi.org/10.1002/adma.201600846.

[73] Y. Tang, W. Zhang, L. Xue, X. Ding, T. Wang, X. Liu, J. Liu, X. Li, Y. Huang, Polypyrrole-promoted superior cyclability and rate capability of $Na_xFe[Fe(CN)_6]$ cathodes for sodium-ion batteries, J. Mater. Chem. A 4 (2016) 6036–6041, https://doi.org/10.1039/c6ta00876c.

[74] W.-J. Li, S.-L. Chou, J.-Z. Wang, J.-L. Wang, Q.-F. Gu, H.-K. Liu, S.-X. Dou, Multifunctional conducing polymer coated $Na_{1+x}MnFe(CN)_6$ cathode for sodium-ion batteries with superior performance via a facile and one-step chemistry approach, Nano Energy 13 (2015) 200–207, https://doi.org/10.1016/j.nanoen.2015.02.019.

[75] H. Wang, L. Wang, S. Chen, G. Li, J. Quan, E. Xu, L. Song, Y. Jiang, Crystallographic-plane tuned prussian-blue wrapped with RGO: a high-capacity, long-life cathode for sodium-ion batteries, J. Mater. Chem. A 5 (2017) 3569–3577, https://doi.org/10.1039/c6ta10592k.

[76] S. Yu, D. Li, Y. Zhang, H. Wang, J. Quan, E. Xu, Y. Jiang, A Na-rich nanocomposite of $Na_{1.83}Ni_{0.12}Mn_{0.88}Fe(CN)_6$/RGO as cathode for superior performance sodium-ion batteries, Nano 13 (2018), https://doi.org/10.1142/s1793292018500649.

[77] P. Nie, L. Shen, G. Pang, Y. Zhu, G. Xu, Y. Qing, H. Dou, X. Zhang, Flexible metal–organic frameworks as superior cathodes for rechargeable sodium-ion batteries, J. Mater. Chem. A 3 (2015) 16590–16597, https://doi.org/10.1039/c5ta03197d.

[78] J. Liu, C. Xu, Z. Chen, S. Ni, Z.X. Shen, Progress in aqueous rechargeable batteries, Green, Energy Environ. 3 (2018) 20–41, https://doi.org/10.1016/j.gee.2017.10.001.

[79] D. Bin, F. Wang, A.G. Tamirat, L. Suo, Y. Wang, C. Wang, Y. Xia, Progress in aqueous rechargeable sodium-ion batteries, Adv. Energy Mater. 8 (2018), https://doi.org/10.1002/aenm.201703008.

[80] X. Shan, D.S. Charles, Y. Lei, R. Qiao, G. Wang, W. Yang, M. Feygenson, D. Su, X. Teng, Bivalence Mn_5O_8 with hydroxylated interphase for high-voltage aqueous sodium-ion storage, Nat. Commun. 7 (2016) 13370, https://doi.org/10.1038/ncomms13370.

[81] J.F. Whitacre, A. Tevar, S. Sharma, $Na_4Mn_9O_{18}$ as a positive electrode material for an aqueous electrolyte sodium-ion energy storage device, Electrochem. Commun. 12 (2010) 463–466, https://doi.org/10.1016/j.elecom.2010.01.020.

[82] Y. Wang, L. Mu, J. Liu, Z. Yang, X. Yu, L. Gu, Y.-S. Hu, H. Li, X.-Q. Yang, L. Chen, X. Huang, A novel high capacity positive electrode material with tunnel-type structure for aqueous sodium-ion batteries, Adv. Energy Mater. 5 (2015), https://doi.org/10.1002/aenm.201501005.

[83] W. Song, X. Ji, Y. Zhu, H. Zhu, F. Li, J. Chen, F. Lu, Y. Yao, C.E. Banks, Aqueous sodium-ion battery using a $Na_3V_2(PO_4)_3$ electrode, ChemElectroChem 1 (2014) 871–876, https://doi.org/10.1002/celc.201300248.

[84] P.R. Kumar, Y.H. Jung, J.E. Wang, D.K. Kim, $Na_3V_2O_2(PO_4)_2$ F-MWCNT nanocomposites as a stable and high rate cathode for aqueous and non-aqueous sodium-ion batteries, J. Power Sources 324 (2016) 421–427, https://doi.org/10.1016/j.jpowsour.2016.05.096.

[85] H. Gao, J.B. Goodenough, An aqueous symmetric sodium-ion battery with NASICON-structured $Na_3MnTi(PO_4)_3$, Angew. Chem. Int. Ed. Engl. 55 (2016) 12768–12772, https://doi.org/10.1002/anie.201606508.

[86] X. Wu, Y. Luo, M. Sun, J. Qian, Y. Cao, X. Ai, H. Yang, Low-defect Prussian blue nanocubes as high capacity and long life cathodes for aqueous Na-ion batteries, Nano Energy 13 (2015) 117–123, https://doi.org/10.1016/j.nanoen.2015.02.006.

[87] B. Paulitsch, J. Yun, A.S. Bandarenka, Electrodeposited $Na_2VO_x[Fe(CN)_6]$ films as a cathode material for aqueous Na-ion batteries, ACS Appl. Mater. Interfaces 9 (2017) 8107–8112, https://doi.org/10.1021/acsami.6b15666.

[88] K. Koshika, N. Sano, K. Oyaizu, H. Nishide, An ultrafast chargeable polymer electrode based on the combination of nitroxide radical and aqueous electrolyte, Chem. Commun. (2009) 836–838, https://doi.org/10.1039/b818087c.

[89] C.D. Wessells, S.V. Peddada, R.A. Huggins, Y. Cui, Nickel hexacyanoferrate nanoparticle electrodes for aqueous sodium and potassium ion batteries, Nano Lett. 11 (2011) 5421–5425, https://doi.org/10.1021/nl203193q.

[90] X. Wu, Y. Cao, X. Ai, J. Qian, H. Yang, A low-cost and environmentally benign aqueous rechargeable sodium-ion battery based on $NaTi_2(PO_4)_3$–$Na_2NiFe(CN)_6$ intercalation chemistry, Electrochem. Commun. 31 (2013) 145–148, https://doi.org/10.1016/j.elecom.2013.03.013.

[91] C.D. Wessells, R.A. Huggins, Y. Cui, Copper hexacyanoferrate battery electrodes with long cycle life and high power, Nat. Commun. 2 (2011) 550, https://doi.org/10.1038/ncomms1563.

[92] X.Y. Wu, M.Y. Sun, Y.F. Shen, J.F. Qian, Y.L. Cao, X.P. Ai, H.X. Yang, Energetic aqueous rechargeable sodium-ion battery based on $Na_2CuFe(CN)_6$-$NaTi_2(PO_4)_3$ intercalation chemistry, ChemSusChem 7 (2014) 407–411, https://doi.org/10.1002/cssc.201301036.

[93] B. Wang, X. Wang, C. Liang, M. Yan, Y. Jiang, An all-prussian-blue-based aqueous sodium-ion battery, ChemElectroChem 6 (2019) 4848–4853, https://doi.org/10.1002/celc.201901223.

[94] W. Li, F. Zhang, X. Xiang, X. Zhang, Nickel-substituted copper hexacyanoferrate as a superior cathode for aqueous sodium-ion batteries, ChemElectroChem 5 (2018) 350–354, https://doi.org/10.1002/celc.201700958.

[95] W. Li, F. Zhang, X. Xiang, X. Zhang, High-efficiency Na-storage performance of a nickel-based ferricyanide cathode in high-concentration electrolytes for aqueous sodium-ion batteries, ChemElectroChem 4 (2017) 2870–2876, https://doi.org/10.1002/celc.201700776.

[96] K. Nakamoto, R. Sakamoto, M. Ito, A. Kitajou, S. Okada, Effect of concentrated electrolyte on aqueous sodium-ion battery with sodium manganese hexacyanoferrate cathode, Electrochemistry 85 (2017) 179–185, https://doi.org/10.5796/electrochemistry.85.179.

[97] K. Nakamoto, R. Sakamoto, Y. Sawada, M. Ito, S. Okada, Over 2 V aqueous sodium-ion battery with prussian blue-type electrodes, Small Methods 3 (2018), https://doi.org/10.1002/smtd.201800220.

[98] J. Wang, C. Mi, P. Nie, S. Dong, S. Tang, X. Zhang, Sodium-rich iron hexacyanoferrate with nickel doping as a high performance cathode for aqueous sodium ion batteries, J. Electroanal. Chem. 818 (2018) 10–18, https://doi.org/10.1016/j.jelechem.2018.04.011.

[99] M. Pasta, R.Y. Wang, R. Ruffo, R. Qiao, H.-W. Lee, B. Shyam, M. Guo, Y. Wang, L. A. Wray, W. Yang, M.F. Toney, Y. Cui, Manganese–cobalt hexacyanoferrate cathodes for sodium-ion batteries, J. Mater. Chem. A 4 (2016) 4211–4223, https://doi.org/10.1039/c5ta10571d.

[100] J.-H. Lee, G. Ali, D.H. Kim, K.Y. Chung, Metal-organic framework cathodes based on a vanadium hexacyanoferrate prussian blue analogue for high-performance aqueous rechargeable batteries, Adv. Energy Mater. 7 (2017), https://doi.org/10.1002/aenm.201601491.

[101] M. Xie, Y. Huang, M. Xu, R. Chen, X. Zhang, L. Li, F. Wu, Sodium titanium hexacyanoferrate as an environmentally friendly and low-cost cathode material for sodium-ion batteries, J. Power Sources 302 (2016) 7–12, https://doi.org/10.1016/j.jpowsour.2015.10.042.

[102] R. Chen, Y. Huang, M. Xie, Q. Zhang, X. Zhang, L. Li, F. Wu, Preparation of prussian blue submicron particles with a pore structure by two-step optimization for Na-ion battery cathodes, ACS Appl. Mater. Interfaces 8 (2016) 16078–16086, https://doi.org/10.1021/acsami.6b04151.

[103] S. Chong, Y. Chen, Y. Zheng, Q. Tan, C. Shu, Y. Liu, Z. Guo, Potassium ferrous ferricyanide nanoparticles as a high capacity and ultralong life cathode material for nonaqueous potassium-ion batteries, J. Mater. Chem. A 5 (2017) 22465–22471, https://doi.org/10.1039/c7ta08139a.

[104] G. He, L.F. Nazar, Crystallite size control of prussian white analogues for nonaqueous potassium-ion batteries, ACS Energy Lett. 2 (2017) 1122–1127, https://doi.org/10.1021/acsenergylett.7b00179.

[105] A. Eftekhari, Potassium secondary cell based on Prussian blue cathode, J. Power Sources 126 (2004) 221–228, https://doi.org/10.1016/j.jpowsour.2003.08.007.

[106] C. Ling, J. Chen, F. Mizuno, First-principles study of alkali and alkaline earth ion intercalation in iron hexacyanoferrate: the important role of ionic radius, J. Phys. Chem. C 117 (2013) 21158–21165, https://doi.org/10.1021/jp4078689.

[107] L. Xue, Y. Li, H. Gao, W. Zhou, X. Lu, W. Kaveevivitchai, A. Manthiram, J. B. Goodenough, Low-cost high-energy potassium cathode, J. Am. Chem. Soc. 139 (2017) 2164–2167, https://doi.org/10.1021/jacs.6b12598.

[108] J.Z. Guo, Z.Y. Gu, X.X. Zhao, M.Y. Wang, X. Yang, Y. Yang, W.H. Li, X.L. Wu, Flexible Na/K-ion full batteries from the renewable cotton cloth-derived stable, low-cost, and binder-free anode and cathode, Adv. Energy Mater. 9 (2019), https://doi.org/10.1002/aenm.201902056.

[109] Y.H. Zhu, Y.B. Yin, X. Yang, T. Sun, S. Wang, Y.S. Jiang, J.M. Yan, X.B. Zhang, Transformation of rusty stainless-steel meshes into stable, low-cost, and binder-free cathodes for high-performance potassium-ion batteries, Angew. Chem. Int. Ed. Engl. 56 (2017) 7881–7885, https://doi.org/10.1002/anie.201702711.

[110] M. Morant-Giner, R. Sanchis-Gual, J. Romero, A. Alberola, L. García-Cruz, S. Agouram, M. Galbiati, N.M. Padial, J.C. Waerenborgh, C. Martí-Gastaldo, S. Tatay, A. Forment-Aliaga, E. Coronado, Prussian blue@MoS_2 layer composites as highly efficient cathodes for sodium- and potassium-ion batteries, Adv. Funct. Mater. 28 (2018), https://doi.org/10.1002/adfm.201706125.

[111] L. Jiang, Y. Lu, C. Zhao, L. Liu, J. Zhang, Q. Zhang, X. Shen, J. Zhao, X. Yu, H. Li, X. Huang, L. Chen, Y.-S. Hu, Building aqueous K-ion batteries for energy storage, Nat. Energy 4 (2019) 495–503, https://doi.org/10.1038/s41560-019-0388-0.

[112] W. Ren, X. Chen, C. Zhao, Ultrafast aqueous potassium-ion batteries cathode for stable intermittent grid-scale energy storage, Adv. Energy Mater. 8 (2018), 1801413, https://doi.org/10.1002/aenm.201801413.

[113] D. Su, A. McDonagh, S.Z. Qiao, G. Wang, High-capacity aqueous potassium-ion batteries for large-scale energy storage, Adv. Mater. 29 (2017), https://doi.org/10.1002/adma.201604007.

[114] X. Wei, J. Wei, Y. Song, D. Wu, X.D. Liu, H. Chen, P. Xiao, Y. Zhang, Potassium mediated Co-Fe-based prussian blue analogue architectures for aqueous potassium-ion storage, Chem. Commun. 57 (2021) 7019–7022, https://doi.org/10.1039/d1cc01852c.

[115] P. Saha, M.K. Datta, O.I. Velikokhatnyi, A. Manivannan, D. Alman, P.N. Kumta, Rechargeable magnesium battery: current status and key challenges for the future, Prog. Mater. Sci. 66 (2014) 1–86, https://doi.org/10.1016/j.pmatsci.2014.04.001.

[116] H.D. Yoo, I. Shterenberg, Y. Gofer, G. Gershinsky, N. Pour, D. Aurbach, Mg rechargeable batteries: an on-going challenge, Energy Environ. Sci. 6 (2013), https://doi.org/10.1039/c3ee40871j.

[117] M. Mao, T. Gao, S. Hou, C. Wang, A critical review of cathodes for rechargeable Mg batteries, Chem. Soc. Rev. 47 (2018) 8804–8841, https://doi.org/10.1039/c8cs00319j.

[118] Y. Mizuno, M. Okubo, E. Hosono, T. Kudo, K. Oh-ishi, A. Okazawa, N. Kojima, R. Kurono, S.-i Nishimura, A. Yamada, Electrochemical Mg^{2+} intercalation into a bimetallic CuFe prussian blue analog in aqueous electrolytes, J. Mater. Chem. A 1 (2013), https://doi.org/10.1039/c3ta13205f.

[119] L. Chen, J.L. Bao, X. Dong, D.G. Truhlar, Y. Wang, C. Wang, Y. Xia, Aqueous Mg-ion battery based on polyimide anode and prussian blue cathode, ACS Energy Lett. 2 (2017) 1115–1121, https://doi.org/10.1021/acsenergylett.7b00040.

[120] A.L. Lipson, S.-D. Han, S. Kim, B. Pan, N. Sa, C. Liao, T.T. Fister, A.K. Burrell, J. T. Vaughey, B.J. Ingram, Nickel hexacyanoferrate, a versatile intercalation host for divalent ions from nonaqueous electrolytes, J. Power Sources 325 (2016) 646–652, https://doi.org/10.1016/j.jpowsour.2016.06.019.

[121] M.S. Chae, J. Hyoung, M. Jang, H. Lee, S.-T. Hong, Potassium nickel hexacyanoferrate as a high-voltage cathode material for nonaqueous magnesium-ion batteries, J. Power Sources 363 (2017) 269–276, https://doi.org/10.1016/j.jpowsour.2017.07.094.

[122] E. Levi, Y. Gofer, D. Aurbach, On the way to rechargeable Mg batteries: the challenge of new cathode materials, Chem. Mater. 22 (2010) 860–868, https://doi.org/10.1021/cm9016497.

[123] P. Novák, J. Desilvestro, Electrochemical insertion of magnesium in metal mxides and sulfides from aprotic electrolytes, J. Electrochem. Soc. 140 (2019) 140–144, https://doi.org/10.1149/1.2056075.

[124] P. Novák, W. Scheifele, F. Joho, O. Haas, Electrochemical insertion of magnesium into hydrated vanadium bronzes, J. Electrochem. Soc. 142 (2019) 2544–2550, https://doi.org/10.1149/1.2050051.

[125] C. Lee, S.-K. Jeong, Modulating the hydration number of calcium ions by varying the electrolyte concentration: electrochemical performance in a prussian blue electrode/aqueous electrolyte system for calcium-ion batteries, Electrochim. Acta 265 (2018) 430–436, https://doi.org/10.1016/j.electacta.2018.01.172.

[126] P. Padigi, G. Goncher, D. Evans, R. Solanki, Potassium barium hexacyanoferrate-a potential cathode material for rechargeable calcium ion batteries, J. Power Sources 273 (2015) 460–464, https://doi.org/10.1016/j.jpowsour.2014.09.101.

[127] L. Zhang, L. Chen, X. Zhou, Z. Liu, Morphology-dependent electrochemical performance of zinc hexacyanoferrate cathode for zinc-ion battery, Sci. Rep. 5 (2015) 18263, https://doi.org/10.1038/srep18263.

[128] M.S. Chae, J.W. Heo, H.H. Kwak, H. Lee, S.-T. Hong, Organic electrolyte-based rechargeable zinc-ion batteries using potassium nickel hexacyanoferrate as a cathode material, J. Power Sources 337 (2017) 204–211, https://doi.org/10.1016/j.jpowsour.2016.10.083.

[129] L.D. Reed, S.N. Ortiz, M. Xiong, E.J. Menke, A rechargeable aluminum-ion battery utilizing a copper hexacyanoferrate cathode in an organic electrolyte, Chem. Commun. 51 (2015) 14397–14400, https://doi.org/10.1039/c5cc06053b.

[130] D. Wang, X. Gao, Y. Chen, L. Jin, C. Kuss, P.G. Bruce, Plating and stripping calcium in an organic electrolyte, Nat. Mater. 17 (2018) 16–20, https://doi.org/10.1038/nmat5036.

[131] R.J. Gummow, G. Vamvounis, M.B. Kannan, Y. He, Calcium-ion batteries: current state-of-the-art and future perspectives, Adv. Mater. 30 (2018), e1801702, https://doi.org/10.1002/adma.201801702.

[132] R.Y. Wang, C.D. Wessells, R.A. Huggins, Y. Cui, Highly reversible open framework nanoscale electrodes for divalent ion batteries, Nano Lett. 13 (2013) 5748–5752, https://doi.org/10.1021/nl403669a.

[133] S. Tobishima, A. Yamaji, Ethylene carbonate—propylene carbonate mixed electrolytes for lithium batteries, Electrochim. Acta 29 (1984) 267–271, https://doi.org/10.1016/0013-4686(84)87058-9.

[134] S.K. Chi, M. Seung, Oh, Importance of donor number in determining solvating ability of polymers and transport properties in gel-type polymer electrolytes, Electrochim. Acta 45.13 (2000) 2101–2109, https://doi.org/10.1016/S0013-4686(99)00426-0.

[135] Y. Yamada, Y. Takazawa, K. Miyazaki, T. Abe, Electrochemical lithium intercalation into graphite in dimethyl sulfoxide-based electrolytes: effect of solvation structure of lithium ion, J. Phys. Chem. C 114 (2010) 11680–11685, https://doi.org/10.1021/jp1037427.

[136] C. Lee, S.-K. Jeong, A novel strategy to improve the electrochemical performance of a prussian blue analogue electrode for calcium-ion batteries, Electrochemistry 86 (2018) 134–137, https://doi.org/10.5796/electrochemistry.17-00069.

[137] T. Tojo, Y. Sugiura, R. Inada, Y. Sakurai, Reversible calcium ion batteries using a dehydrated prussian blue analogue cathode, Electrochim. Acta 207 (2016) 22–27, https://doi.org/10.1016/j.electacta.2016.04.159.

[138] Z. Liu, G. Pulletikurthi, F. Endres, A prussian blue/zinc secondary battery with a bio-ionic liquid-water mixture as electrolyte, ACS Appl. Mater. Interfaces 8 (2016) 12158–12164, https://doi.org/10.1021/acsami.6b01592.

[139] R. Trocoli, F. La Mantia, An aqueous zinc-ion battery based on copper hexacyanoferrate, ChemSusChem 8 (2015) 481–485, https://doi.org/10.1002/cssc.201403143.

[140] L. Zhang, L. Chen, X. Zhou, Z. Liu, Towards high-voltage aqueous metal-ion batteries beyond 1.5 V: the zinc/zinc hexacyanoferrate system, Adv. Energy Mater. 5 (2015), https://doi.org/10.1002/aenm.201400930.

[141] Y. Gao, H. Yang, X. Wang, Y. Bai, N. Zhu, S. Guo, L. Suo, H. Li, H. Xu, C. Wu, The compensation effect mechanism of Fe-Ni mixed prussian blue analogues in aqueous rechargeable aluminum-ion batteries, ChemSusChem 13 (2020) 732–740, https://doi.org/10.1002/cssc.201903067.

[142] Y. Ru, S. Zheng, H. Xue, H. Pang, Potassium cobalt hexacyanoferrate nanocubic assemblies for high-performance aqueous aluminum ion batteries, Chem. Eng. J. 382 (2020), https://doi.org/10.1016/j.cej.2019.122853.

[143] L. Chen, Q. An, L. Mai, Recent advances and prospects of cathode materials for rechargeable aqueous zinc-ion batteries, Adv. Mater. Interfaces 6 (2019), https://doi.org/10.1002/admi.201900387.

[144] D. Selvakumaran, A. Pan, S. Liang, G. Cao, A review on recent developments and challenges of cathode materials for rechargeable aqueous Zn-ion batteries, J. Mater. Chem. A 7 (2019) 18209–18236, https://doi.org/10.1039/c9ta05053a.

[145] W. Deng, Z. Li, Y. Ye, Z. Zhou, Y. Li, M. Zhang, X. Yuan, J. Hu, W. Zhao, Z. Huang, C. Li, H. Chen, J. Zheng, R. Li, Zn^{2+} Induced phase transformation of $K_2MnFe(CN)_6$ boosts highly stable zinc-ion storage, Adv. Energy Mater. 11 (2021), https://doi.org/10.1002/aenm.202003639.
[146] G. Ni, X. Xu, Z. Hao, W. Wang, C. Li, Y. Yang, C. Zhou, L. Qin, W. Chen, X. Yao, J. Cai, Tuning the electrochemical stability of zinc hexacyanoferrate through manganese substitution for aqueous zinc-ion batteries, ACS Appl. Energy Mater. 4 (2020) 602–610, https://doi.org/10.1021/acsaem.0c02496.
[147] Q. Li, K. Ma, G. Yang, C. Wang, High-voltage non-aqueous $Zn/K_{1.6}Mn_{1.2}Fe(CN)_6$ batteries with zero capacity loss in extremely long working duration, Energy Storage Mater. 29 (2020) 246–253, https://doi.org/10.1016/j.ensm.2020.04.030.
[148] L. Ma, S. Chen, C. Long, X. Li, Y. Zhao, Z. Liu, Z. Huang, B. Dong, J.A. Zapien, C. Zhi, Achieving high-voltage and high-capacity aqueous rechargeable zinc ion battery by incorporating two-species redox reaction, Adv. Energy Mater. 9 (2019), https://doi.org/10.1002/aenm.201902446.
[149] V. Verma, S. Kumar, W. Manalastas, R. Satish, M. Srinivasan, Progress in rechargeable aqueous zinc- and aluminum-ion battery electrodes: challenges and outlook, Adv. Sustain. Syst. 3 (2019), https://doi.org/10.1002/adsu.201800111.
[150] S. Liu, G.L. Pan, G.R. Li, X.P. Gao, Copper hexacyanoferrate nanoparticles as cathode material for aqueous Al-ion batteries, J. Mater. Chem. A 3 (2015) 959–962, https://doi.org/10.1039/c4ta04644g.
[151] F. Wu, H. Yang, Y. Bai, C. Wu, Paving the path toward reliable cathode materials for aluminum-ion batteries, Adv. Mater. 31 (2019), e1806510, https://doi.org/10.1002/adma.201806510.
[152] J. Peng, W. Zhang, Q. Liu, J. Wang, S. Chou, H. Liu, S. Dou, Prussian blue analogues for sodium-ion batteries: past, present, and future, Adv. Mater. 34 (2022), https://doi.org/10.1002/adma.202108384.
[153] G. Du, H. Pang, Recent advancements in prussian blue analogues: preparation and application in batteries, Energy Storage Mater. 36 (2021), https://doi.org/10.1016/j.ensm.2021.01.006.
[154] H. Yi, R. Qin, S. Ding, Y. Wang, S. Li, Q. Zhao, F. Pan, Structure and properties of prussian blue analogues in energy storage and conversion applications, Adv. Funct. Mater. 31 (2020), https://doi.org/10.1002/adfm.202006970.
[155] A. Mohammad, Y. Yang, M.A. Khan, P.J. Faustino, Long-term stability study of prussian blue-a quality assessment of water content and cyanide release, J. Pharm. Biomed. 53 (2015) 102–107, https://doi.org/10.3109/15563650.2014.998337.
[156] Y. Yang, C. Brownell, N. Sadrieh, J. May, A. Del, Quantitative measurement of cyanide released from Prussian Blue, Clin. Toxicol. 45 (2007) 776–781, https://doi.org/10.1080/15563650601181562.
[157] C. Aparicio, L. Machala, Z. Marusak, Thermal decomposition of Prussian blue under inert atmosphere, J. Therm. Anal. Calorim. 110 (2011) 661–669, https://doi.org/10.1007/s10973-011-1890-1.
[158] H. Inoue, T. Nakazawa, T. Mitsuhashi, T. Shirai, E. Fluck, Characterization of Prussian Blue and Its Thermal Decomposition Products, 1989. ⟨https://doi.org/10.1007/bf02398265⟩.
[159] A. Kwade, Challenges in ecofriendly battery recycling and closed material cycles: a perspective on future lithium battery generations, Metals 11 (2021), https://doi.org/10.3390/met11020291.
[160] O. Velázquez-Martínez, J. Valio, A. Santasalo-Aarnio, M. Reuter, R. Serna-Guerrero, A critical review of lithium-ion battery recycling processes from a circular economy perspective, Batteries 5 (2019), https://doi.org/10.3390/batteries5040068.
[161] M. Sommerfeld, C. Vonderstein, C. Dertmann, J. Klimko, B. Friedrich, A combined pyro- and hydrometallurgical approach to recycle pyrolyzed lithium-ion battery black mass part 1: production of lithium concentrates in an electric arc furnace, Metals 10 (2020), https://doi.org/10.3390/10.3390/met10081069.
[162] Zhang Lei, Bin Hao, Srinivasan Wu, Huey Madhavi, Hng Hoon, Formation of Fe_2O_3 microboxes with hierarchical shell structures from metal–organic frameworks and their lithium storage properties, J. Am. Chem. Soc. 134 (2012) 17388–17391, https://doi.org/10.1021/ja307475c.
[163] A.R. Yeddou, B. Nadjemi, F. Halet, A. Ould-Dris, R. Capart, Removal of cyanide in aqueous solution by oxidation with hydrogen peroxide in presence of activated carbon prepared from olive stones, Miner. Eng. (2010), https://doi.org/10.1016/j.mineng.2009.09.009.
[164] J. Peng, W. Zhang, J. Wang, L. Li, S.X. Dou, Processing rusty metals into versatile prussian blue for sustainable energy storage, Adv. Energy Mater. ⟨https://doi.org/10.21203/rs.3.rs-361418/v1⟩.

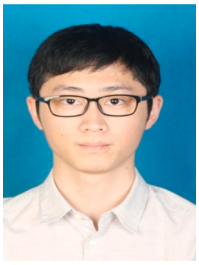

Yujie Yang received his Bachelor degree from Shanghai Polytechnic University, Shanghai in 2019. At present, he is pursuing his Master of Engineering in Shanghai University. His current research focuses on Lithium-ion Battery and Potassium-ion Battery.

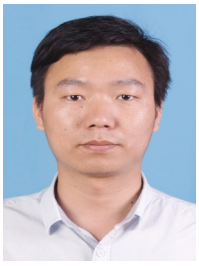

Jianbin Zhou received his Ph.D. degree in Nanochemistry from the Hefei National Laboratory for Physical Sciences at the Microscale, University of Science and Technology of China, in June 2017. After that, he worked as a post-doctoral researcher at the University of Science and Technology of China and Pacific Northwest National Laboratory (USA). His research is focused on developing high performance all solid state batteries and synthesis of nanomaterials.

Linlin Wang received her Ph.D. in inorganic chemistry in 2013 from the University of Science and Technology of China (USTC) under the direction of Prof. Kai-bin Tang and Prof. Yi-tai Qian. She was selected for the Shanghai Sailing Program in 2014. She is currently a full *associate* professor at Shanghai University. Her current focus is on advanced materials for electrochemical energy storage and conversion, including electrodes in Li/Na/K-ion batteries and electrocatalysis in fuel cells.

Zheng Jiao is a professor at School of Environmental and Chemical Engineering, Shanghai University and Executive Deputy Director of Key Laboratory of Organic Compound Pollution Control Engineering, Ministry of Education. Pro. Jiao received his Ph.D. from University of Science and Technology of China in 2000. He was a COE research fellow at Institute of Industrial Science, Osaka University, Japan from 2002 to 2003 and a postdoctoral fellow at University of Technology, Lille, France in 2004. His research interests focus on the control synthesis, mechanism and application of environmental functional materials and new energy materials.

Meiyi Xiao is a sophomores of Shanghai University. she is currently studying chemical technology and engineering.

Qiu-an Huang is currently an associate professor at Institute for Sustainable Energy/ College of Science, Shanghai University, China. In 07/1997–10/2018, he worked at Faculty of Electronic Engineering, Hubei University. He received B.Sc. in 1997 from Beijing University of Chemical Technology (BUCT), M.Sc in 2004 and Ph.D in 2009 both from Huazhong University of Science and Technology (HUST), China, all majored in Control Theory and Control Engineering. His research interest mainly focused on EIS theoretical modeling/simulating, fast measurement/identification, and intelligent diagnosis/analysis for electrochemical energy storage and conversion technique.

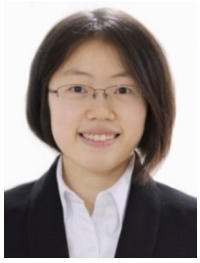

Minmin Liu received her Ph.D. in Analytic Chemistry from Changchun Institute of Applied Chemistry (CIAC), Chinese Academy of Sciences (CAS) under the direction of Professor Wei Chen in 2016. She was selected for Shanghai Sailing Program in 2018. She is a lecturer in Institute for Sustainable Energy/College of Sciences, Shanghai University. Her research interest focus on the design and application of advanced nanomaterial electrocatalysts for electrochemical energy storage and conversion, including CO_2 electrolysis, fuel cells and batteries, etc.

Qinsi Shao is now an assistant researcher at Shanghai University. She received her Bachelor's degree in Materials Science and Engineering from Shandong University, and her Ph.D. in Materials Science from Shanghai University. Her research interests are in the areas of carbon materials, fibers, and electroplating.

Prof. Xueliang Sun is the Canada Research Chair in Development of Nanomaterials for Clean Energy, a Fellow of the Royal Society of Canada and Canadian Academy of Engineering and a Full Professor at the University of Western Ontario, Canada. Dr. Sun received his Ph.D. in 1999 from the University of Manchester, UK, which he followed up by working as a postdoctoral fellow at the University of British Columbia, Canada, and as a Research Associate at L′ Institut National de la Recherche Scientifique (INRS), Canada. His current research interests are focused on advanced materials for electrochemical energy storage and conversion.

Prof. Jiujun Zhang is a Professor in the College of Sciences/ Institute for Sustainable Energy at Shanghai University, a former Principal Research Officer at the National Research Council of Canada (NRC). Dr. Zhang is a Fellow of the Canadian Academy of Engineering (CAE), Fellow of The Academy of Science of The Royal Society of Canada (FRSCCA). Dr. Zhang received his B.S. and M.Sc. in electrochemistry from Peking University in 1982 and 1985, respectively, and his Ph.D. in Electrochemistry from Wuhan University in 1988. Dr. Zhang's main research areas are electrochemistry, electrocatalysts, fuel cells, lithium batteries, metal-air batteries, supercapacitors, and H_2O/CO_2 electrolysis.